EVALUATION OF SHEAR-WAVE VELOCITY PREDICTION MODELS AT NORNE FIELD, NORWEGIAN SEA

A Thesis

Presented to

the Faculty of the Department of Earth and Atmospheric Science

University of Houston

In Partial Fullfillment

of the Requirements for the Degree

Master of Science

By

Tommy Ringo

August, 2012

EVALUATION OF SHEAR-WAVE VELOCITY PREDICTION MODELS AT NORNE FIELD, NORWEGIAN SEA

_____

Tommy Ringo

APPROVED:

_____

Dr. Evgeni Chesnokov

_____

Dr. Robert Stewart

_____

Dr. Colin Sayers

_____

Dean, College of Natural Science and Mathematics

ACKNOWLEDGEMENTS

I would like to thank Dr. Evgeni Chesnokov, Dr. Robert Stewart, and Dr. Colin Sayers for serving on my committee. Special thanks go to my fellow student, Luanxiao Zhao, for his greatly appreciated assistance with coding and his enlightening discussions. Finally, I would like to thank my wife, Priscilla, for her unwavering support and patience during my graduate studies.

EVALUATION OF SHEAR-WAVE VELOCITY PREDICTION MODELS AT NORNE FIELD, NORWEGIAN SEA

An Abstract of a Thesis

Presented to

the Faculty of the Department of Earth and Atmospheric Science

University of Houston

In Partial Fullfillment

of the Requirements for the Degree

Master of Science

By

Tommy Ringo

August, 2012

Abstract

Several shear-wave velocity (Vs) prediction models have been tested on wireline log data at Norne Field in the Norwegian Sea. A genetic algorithm was used to invert P-wave velocity (Vp) for the elastic parameters using the Krief, Self-consistent (SC), and Differential Effective Medium (DEM) models. The inverted shear moduli were then used to predict Vs. Using this method, the Krief method provided the best match of the effective medium models to the measured Vs. Error analysis shows that the predicted Vs is largely correlated with Vp, density, and porosity. Higher Vp, higher density, and lower porosity tend to produce the largest prediction error.

These predictions were compared to other well-established Vs prediction models and the effect of these predictions on AVO modeling was investigated. It is shown that the AVO response begins to show noticeable difference at small Vs errors. For example, the DEM prediction at the oil saturated well had a 6.8% error from the measured Vs at the AVO modeled interval, and AVO mismatch begins at around 15 degrees offset. At the brine saturated well, the Krief, Greenberg-Castagna, and Raymer-Hunt-Gardner (RHG) Vs predictions provided the closest match to the true AVO model while at the oil saturated well, the Krief, RHG, and Han Vs predictions provided the best match to the true AVO model.

Table of Contents

Chapter 1: Introduction

Reservoir characterization and amplitude variation with offset (AVO) studies require accurate shear-wave velocities (Vs) to properly interpret the area of study. Vp/Vs ratios can be used to identify lithology, or identify hydrocarbon bearing formations, and inaccurate Vs can give misleading results. Often, especially in older wells, Vs data are missing or of poor quality. Instead of conducting an expensive logging run to acquire Vs data, a Vs log is often predicted using various methods. These Vs prediction techniques mostly involve (1) effective medium models, (2) heuristic models, or (3) empirical models (Smith, 2011). The empirical models are the easiest to apply; however, there is no way to check their accuracy if predicting a single well, and many of them have been derived in only brine-saturated environments. On the other hand, the effective medium and heuristic models are applicable to a larger range of environments but require as inputs various parameters that may be difficult to obtain. Also, many of these models were derived in the laboratory and their effectiveness in predicting a Vs log has limited investigation.

The objective of this thesis is to evaluate several of these Vs prediction models on wireline log data and quantify their effect on AVO modeling. The data used in this study consist of log data, provided by Statoil, from two wells in the Norne Field, a sandstone reservoir below the Norwegian Sea in about 370 meters of water. The first well, which will be called well #1, is brine saturated with a depth interval of 2676-2837 m true vertical depth (TVD). Available logs include:

- Gamma Ray (GR)

- Shale Volume (Vshale)
- Density Porosity (Phid)
- Neutron Porosity (Nphi)
- Water Saturation (Sw)
- Bulk Density (Rhob)
- Compressional-wave Slowness (DTC)
- Shear-wave Slowness (DTS)

Slowness has been converted to velocity. Well #2 ranges in depth from 2597-2791 m TVD. It contains oil with an oil-water contact at 2694.7 m TVD. The same logs available in well #1 are available in well #2. The suite of logs for each well are shown in figures 1 and 2. The methods and parameters used by Statoil to derive the petrophysical parameters are shown in appendix A.

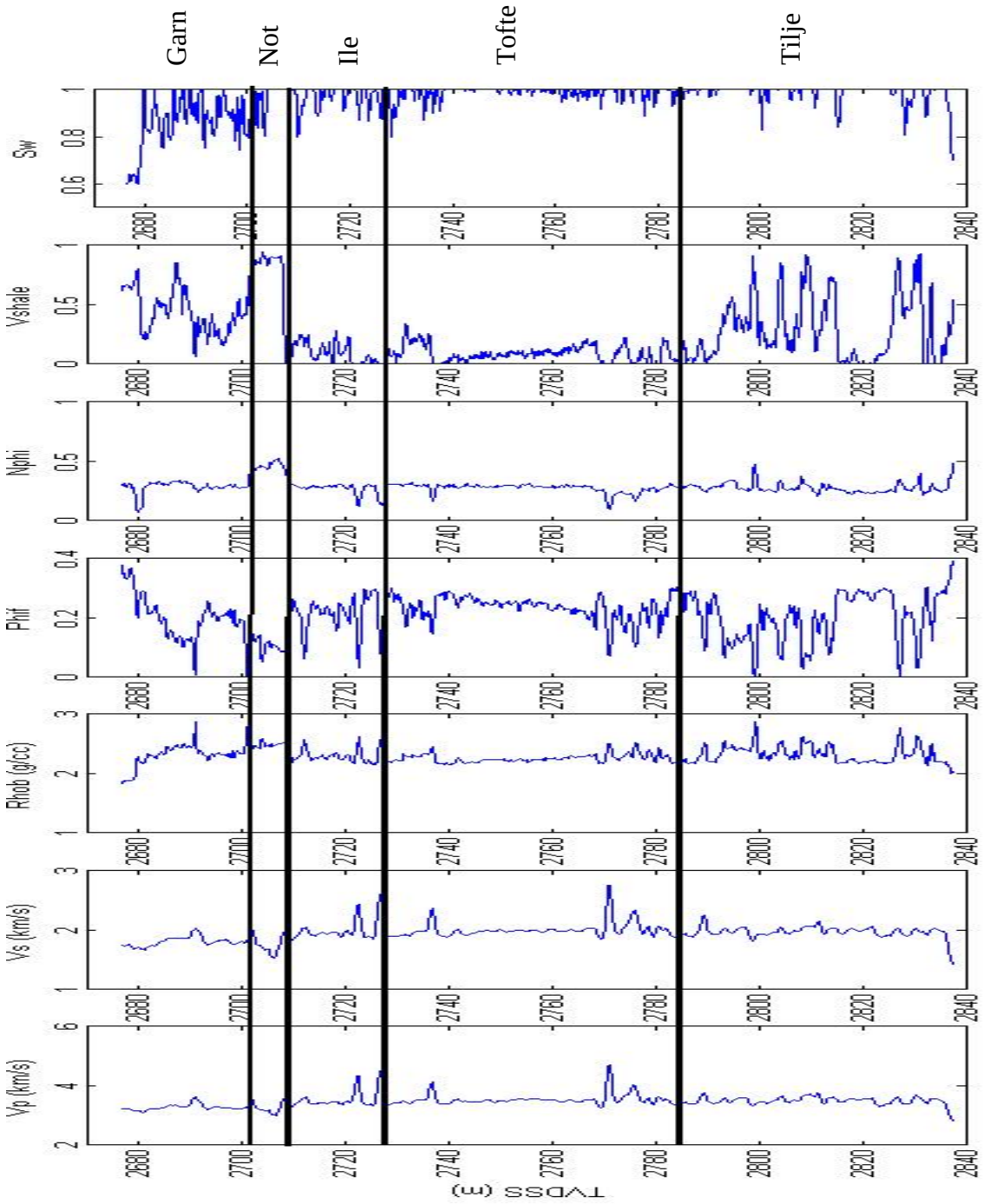

Figure 1: Well log suite for well #1. Major formations are delineated by the black lines.

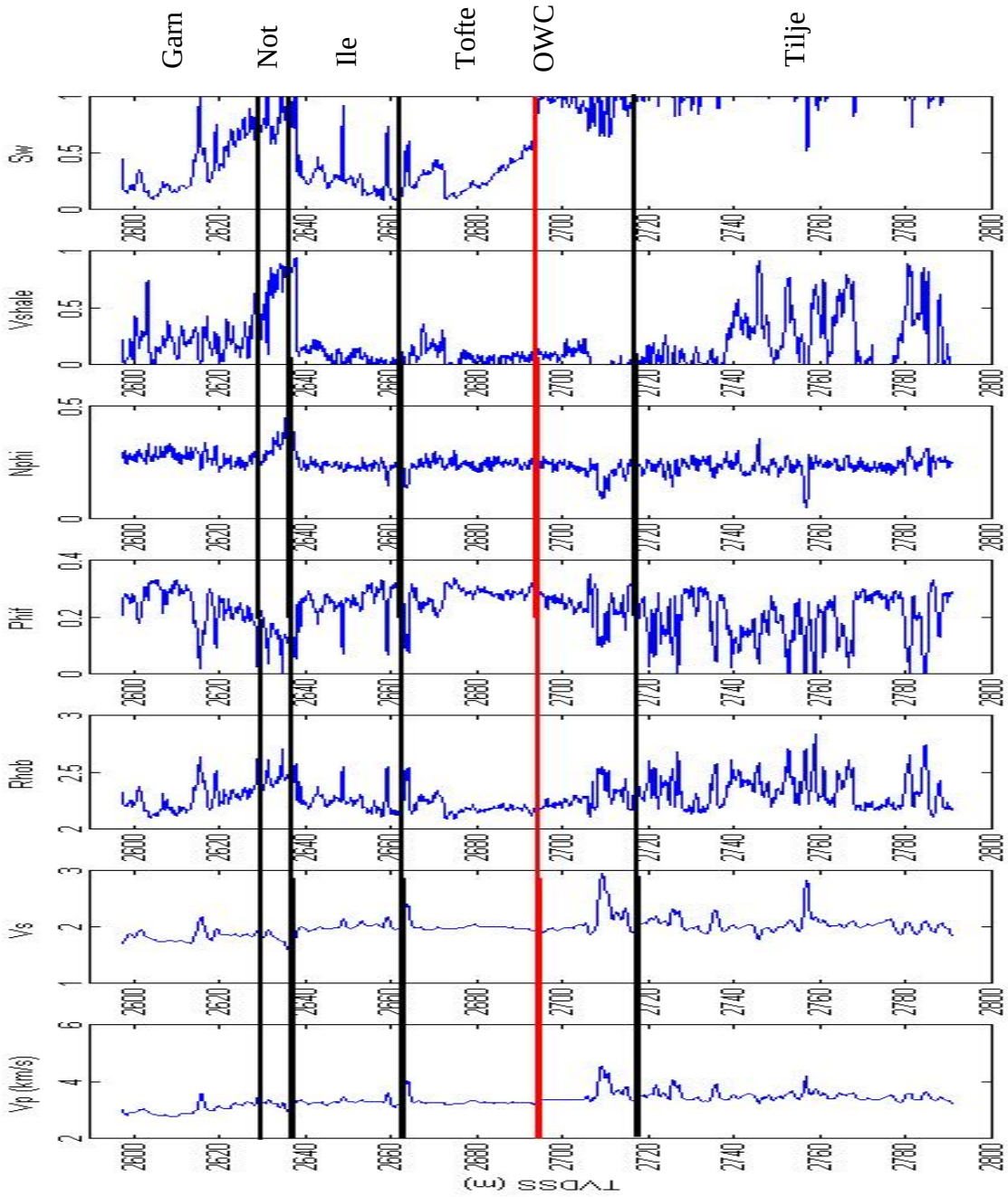

Figure 2: Well log suite for well #2. Major formations are delineated by the black lines. The oil-water contact (OWC) is shown is indicated by the red line.

Chapter 2: Geologic Setting

The Norne Field is located 200 km offshore on the Norwegian continental shelf in water depths of 370-390 m (Steffensen and Karstad, 1996). The field was discovered in 1991 with a 110 m column of oil and a 25 m gas cap. Figure 3 gives well locations and hydrocarbon distribution within the field. The field is part of a horst structure that is 9 km x 3 km and the top of the reservoir lies at 2525 m mean sea level. The reservoir is composed of Jurassic sandstones and is divided into 4 main formations, from top to base: Garn, Ile, Tofte, and Tilje. These sands are classified as mostly fine-grained, well to very well sorted subarkosic arenites (Verlo and Hetland, 2008). Separating the Garn and Ile formations is the Not claystone which acts as a pressure barrier between the units.

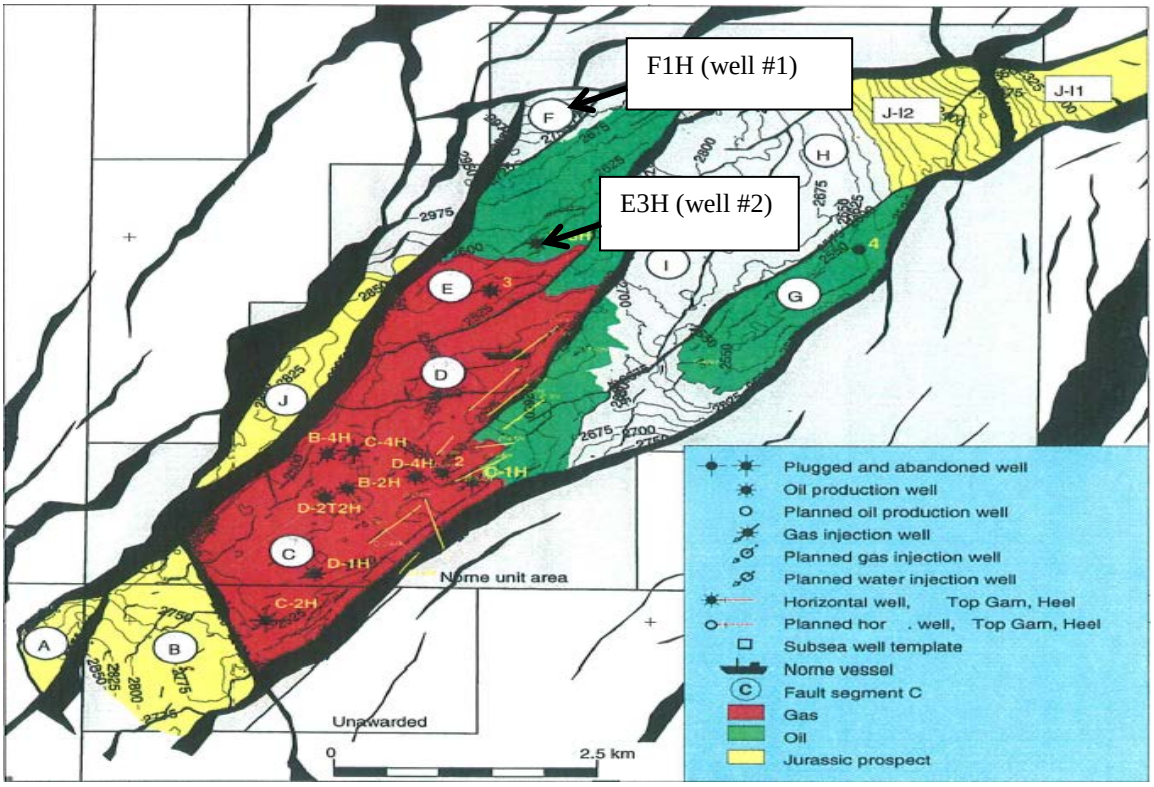

Figure 3: Well locations and hydrocarbon distribution within Norne Field. Red is gas and green is oil. Locations of the wells used in this study are marked. (Statoil, 1999)

The reservoir becomes thinner to the north due to erosion and thickness varies in the field from 260 m in the south to 120 m in the north. Thicknesses of the total reservoir in this study are 165 m at well #1 and 195 m at well #2. Detailed descriptions of the reservoir formations are provided in the following.

2.1 Garn Formation

The Garn formation sits on top of the Not formation and represents the shallowest formation in the reservoir. It is subdivided into 3 compartments based on differing properties and reservoir quality increases from the bottom to the top. Garn 1, the

lowermost portion of the Garn formation, is a sandstone that coarsens upwards. The bottom of Garn 1 is muddy and bioturbated, as it is an extension of the Not formation, and sand content increases upward. Garn 2 consists of fine-grained sandstone and has a calcareous cement at the top which can act as a local barrier to fluid flow (Verlo and Hetland, 2008). Garn 3 is made up of cross-bedding and fine-grained sandstone sitting below a coarse-grained sandstone.

2.2 Not Formation

The Not formation is a dark gray to black claystone deposited in a quiet marine environment. The formation coarsens upward into the Garn formation and actually a very fine-grained, bioturbated sandstone is present at the top of the formation.

2.3 Ile Formation

The Ile formation was deposited at the shoreface and is subdivided into three sections. Ile 1 and 2 are separated by a calcareous cemented layer while Ile 2 and 3 are separated by a sequence boundary, indicating a shift from a regressive to transgressive environment (Verlo and Hetland, 2008). Ile 1 and 2 are composed of fine- to very fine-grained sand which coarsens to the north. Ile 3 is a heavily bioturbated, fine- to very fine-sandstone that fines upwards.

2.4 Tofte Formation

The Tofte formation sits on top of an unconformity that represents a hiatus most likely due to uplift and subsequent aerial exposure and erosion (Verlo and Hetland, 2008). This formation was deposited in a marine environment from foreshore to offshore and is subdivided into three sections. Tofte 1 is bioturbated and fine grained at the bottom

and coarsens upward into a medium to coarse-grained sandstone. Tofte 2 is a heavily bioturbated, muddy and fine-grained sandstone while Tofte 3 is a fine- to very fine-grained sandstone which is also heavily bioturbated. A coarser grained bed is found at the top of the Tofte formation and represents a sequence boundary.

2.5 Tilje Formation

The Tilje formation sits below the aforementioned unconformity and was deposited in a tidally affected environment. It consists mostly of sandstone with some claystone and conglomerates and is subdivided into four sections. Tilje 1 is believed to be composed of two sandstone sections, one coarsening upward and a massive sandstone on top. Tilje 2 is a heterolithic unit consisting of sandy layers, bioturbated shales, laminated shales, and conglomeratic sections. Tilje 3 is a fine-grained sandstone with low bioturbation while Tilje 4 is composed of a fine-grained, bioturbated, muddy sandstone in the lower section and conglomeratic layers interbedded with sandstone and shale.

Chapter 3: Methods

3.1 Inversion Scheme

Chaveste and Jimenez (2003) presented a technique to determine the elastic moduli and densities of rocks by minimizing the difference between the measured and modeled P- and S-wave velocities and density. Rock properties are often assumed for log data, however, these chosen values may not be representative of the true conditions. For example, typical values of bulk modulus and shear modulus for quartz are 37 and 44, respectively, but these values may be inappropriate to the conditions of the area of study.

First, the velocities are modeled by representing Vp and Vs as:

$$Vp = \sqrt{\frac{K_{sat} + \frac{4}{3}\mu_{sat}}{\rho_{sat}}} \qquad (1a)$$

and

$$Vs = \sqrt{\frac{\mu_{sat}}{\rho_{sat}}} \qquad (1b)$$

where K_{sat} and μ_{sat} are the saturated bulk and shear moduli, respectively, and ρ_{sat} is the saturated density. The density can be estimated by a weighted sum of the rock constituents:

$$\rho = \sum_i f_i * \rho_i \qquad (2)$$

where f_i is the volume fraction of the i^{th} component and ρ_i is its density. K_{sat} is estimated from Gassmann's equation (Gassmann, 1951) which can be represented as (Smith, 2003):

$$K_{sat} = K^* + \frac{\left(1 - \frac{K^*}{K_0}\right)^2}{\frac{\emptyset}{K_{fl}} + \frac{(1-\emptyset)}{K_0} - \frac{K^*}{K_0^2}} \quad (3)$$

where K* =the dry frame bulk modulus, K_0 = the bulk modulus of the mineral matrix, K_{fl} = the pore fluid bulk modulus, and $\emptyset$ = porosity. According to the Gassmann formulation, the shear modulus is insensitive to the pore fluid and thus:

$$\mu_{sat} = \mu_{dry} \quad (4)$$

The bulk and shear moduli of the mineral matrix can be estimated by Voigt-Reuss-Hill averaging:

$$M_{k,\mu} = \frac{1}{2}(M_V + M_R) \quad (5a)$$

where M_V is the Voigt bound given as:

$$M_V = \sum_{i=1}^{n} f_i M_i \quad (5b)$$

and M_R is the Reuss bound given as:

$$\frac{1}{M_R} = \sum_{i=1}^{n} \frac{f_i}{M_i} \quad (5c)$$

where f_i = the volume of the i^{th} mineral and M_i = its respective modulus. The bulk modulus of the fluid, K_{fl}, can be calculated by Wood's relation (Wood, 1955):

$$\frac{1}{K_{fl}} = \frac{S_w}{K_w} + \frac{(1 - S_w)}{K_{hyc}} \quad (6)$$

where S_w = the water saturation, K_w = the bulk modulus of water, and K_{hyc} = the hydrocarbon bulk modulus. The bulk moduli of the pore fluids at reservoir conditions can

be calculated by the Batzle and Wang formulation (Batzle and Wang, 1992). Finally, the dry frame bulk modulus can be calculated based on the chosen model.

An objective function can now be minimized to solve for the various constants that make up the previous equations. The objective function to be minimized is (Chaveste and Hilterman, 2007):

$$OF = \left[W_{V_p} \sum (Vp_e - Vp_m)^2 + W_{V_s} \sum (Vs_e - Vs_m)^2 + W_\rho \sum (\rho_e - \rho_m)^2 \right] \quad (7)$$

where e represents the estimated value and m represents the measured value. W is a weighting factor that is a function of the reciprocal of the standard deviation of the respective parameter.

This method can be used for Vs prediction by setting $W_{Vs} = 0$ and using the inverted shear modulus from V_p in equation (1b). In this study, density was decoupled from the objective function and thus the equation to be minimized is:

$$OF = \sum (Vp_e - Vp_m)^2 \quad (8)$$

This objective function provides the basis for Vs prediction using effective medium models in this study. The effective medium models presented in the following sections were tested using this method by solving for the dry frame Vp and performing Gassmann fluid substitution to reservoir conditions using equation (3).

A genetic algorithm in MATLAB is used to solve for the objective function. Genetic algorithms can solve constrained and unconstrained problems and are based on the biological principle of natural selection (MATLAB user's guide). Whereas classical optimization routines generate a single point at each iteration, genetic algorithms generate

populations of points with the best point approaching the optimal solution. The algorithm evolves over generations to an optimal solution and stops based on defined stopping criteria. The stopping criteria in this study is a minimum change in the fitness (objective) function value of 1e-6 from one generation to the next. Figure 4 shows the results of using a genetic algorithm and an objective function as described above to invert for grain densities (in this case, sand and shale). We can see that this method works exceptionally well for inverting for grain densities.

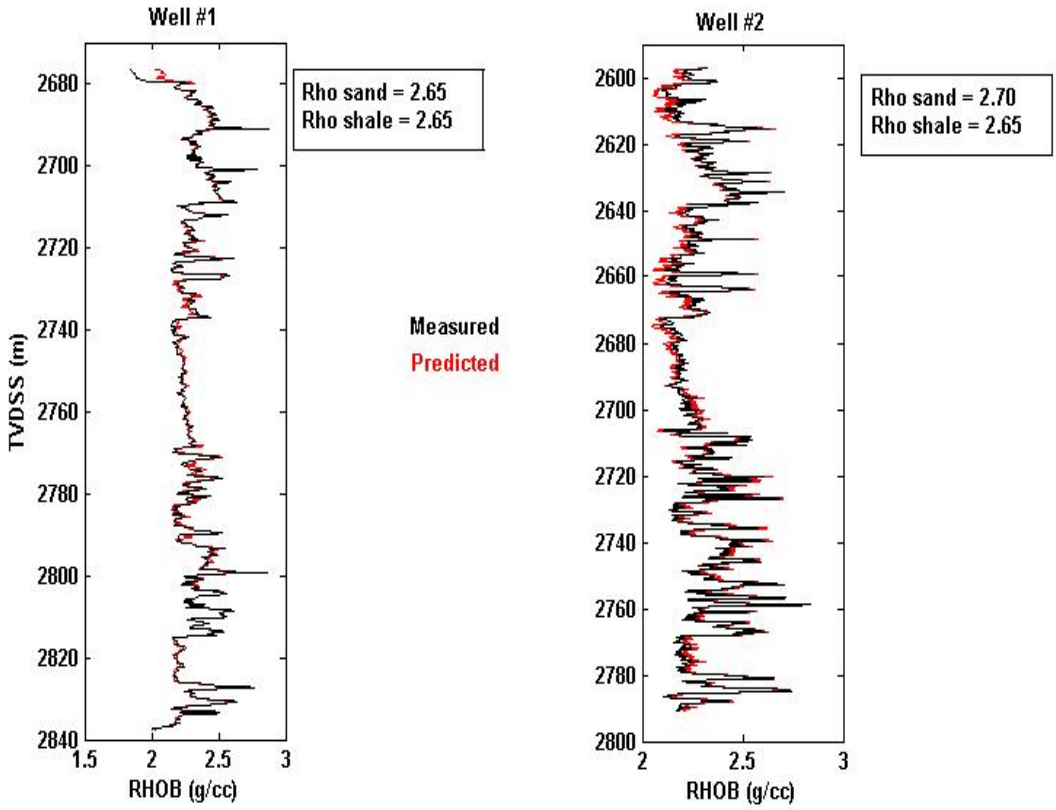

Figure 4: Measured Vs. Predicted bulk densities using the inverted sand and shale grain densities.

3.2 Shear-wave Velocity Predictors

3.2.1 Krief Method

Krief et al., (1990) developed a method of relating the dry frame moduli to the mineral matrix moduli, porosity, and the Biot coefficient. Their formulas originate with the equation of the dry frame bulk modulus given in Gassmann (1951). The resulting equations for the dry frame bulk modulus and shear modulus are:

$$K_{dry} = K_0(1-\beta) \tag{9a}$$

and

$$\mu_{dry} = \mu_0(1-\beta) \tag{9b}$$

where β = the Biot coefficient. They equated (1-β) to $(1-\phi)^m$ and found m = 3/(1-ϕ) by a best fit to the data. The final versions of equations (9a) and (9b) are:

$$K_{dry} = K_0(1-\emptyset)^{\frac{3}{(1-\emptyset)}} \tag{10a}$$

and

$$\mu_{dry} = \mu_0(1-\emptyset)^{\frac{3}{(1-\emptyset)}} \tag{10b}$$

(10a,b) are input to equations (3) and (4) and the genetic algorithm is used to solve for the bulk and shear moduli of sand and shale denoted as K_{sand}, μ_{sand}, K_{shale}, and μ_{shale}, respectively. The inverted shear moduli are then used in equation (1b) to estimate Vs.

3.2.2 Self-consistent (SC) Effective Medium Method

Several frequently used elastic moduli estimation methods (the Hashin-Shtrikman and Voigt-Reuss bounding methods, for example) are based on the moduli and the

volume fractions of each constituent. However, it has been shown that the geometry of the components plays an important role in their elastic moduli; therefore, methods have been developed that take into account the shapes of the inclusions. Most of these methods solve for the elastic deformation of an inclusion of one material in an infinite background host and then estimate the elastic moduli when there is a distribution of these inclusions (Mavko, 2009). The downfall of these methods is that they only are applicable to dilute concentrations of inclusions and thus may not be applicable to the given conditions. For example, the Kuster-Toksoz model is only applicable to situations where (Xu and White, 1995):

$$\frac{\emptyset}{\alpha} \ll 1$$

where α is the aspect ratio of the inclusions. One method for accounting for the interaction of inclusions is the self-consistent (SC) approximation. This method replaces the background medium with a new background medium after inclusions have been added and is solved iteratively until the total volume of inclusions has been added. One major difference between this model and the DEM model described in the next section is that the SC model does not treat any of the individual constituents as the host medium. Berryman (1980) provided a general solution to the original self-consistent formulation for a medium with N-phases:

$$\sum_{i=1}^{N} x_i (K_i - K_{sc}^*) P^{*i} = 0 \qquad (11a)$$

and

$$\sum_{i=1}^{N} x_i(\mu_i - \mu_{sc}^*)\, Q^{*i} = 0 \qquad (11b)$$

where x_i = the volume fraction of the i^{th} phase, K_i,μ_i = the bulk and shear modulus of the i^{th} phase, respectively, K_{sc},μ_{sc} = the effective moduli of the self-consistent background medium, and P,Q = geometric factors. The expressions for P and Q are given in Appendix B. This method includes the shape of the grains as well as the shapes of the inclusions. Equations (11a) and (11b) are solved for dry inclusions by setting K and $\mu = 0$ for the inclusion phases. Saturated moduli can be estimated with this method, however, the model assumes inclusion isolation with respect to pore flow and thus is appropriate to high-frequency laboratory conditions. For logging frequencies, it is better to solve for dry frame elastic moduli and then use Gassmann's equation to fill the pores with the applicable fluid (Mavko et al., 2009).

3.2.3 Differential Effective Medium (DEM) Method

An alternative effective medium method that takes into account the geometry of the components and allows for more than a dilute concentration of inclusions is the differential effective medium (DEM) method. Whereas the self-consistent method applied to a composite of an N number of phases, DEM is restricted to a 2-phase medium. Phase 1 (the matrix) begins with no inclusions, and phase 2 (the inclusions) are incrementally added to phase 1. This process continues until the desired fraction of the inclusion phase is reached, in this case porosity. In reality, the evolution of a rock'sporosity may not occur in this manner and thus this is merely a thought experiment

and should not be taken to represent the true nature of the porosity evolution (Mavko, 2009).

Berryman (1992) gave the formulation for the differential equations used to solve for the effective bulk and shear moduli as:

$$(1-y)\frac{d}{dy}[K^*(y)] = (K^2 - K^*)P^{*2}(y) \qquad (12a)$$

and

$$(1-y)\frac{d}{dy}[\mu^*(y)] = (\mu^2 - \mu^*)Q^{*2}(y) \qquad (12b)$$

where K* and μ* are the effective moduli, K^2 and μ^2 = the bulk and shear moduli of the inclusions, y = the inclusion volume (porosity in this study), and P and Q = geometric factors as described in appendix B. As with the self-consistent method, dry moduli are first estimated by setting K* and μ* = 0 and the saturated moduli are estimated by Gassmann's equation. The reason for this arises from the same frequency stipulation mentioned for the self-consistent method.

3.2.4 The Mudrock Line

Castagna et al. (1985) define a mudrock as a clastic, silicate rock composed mainly of clay or silt-sized grains. They found an empirical relationship between the compressional velocity and shear velocity of water-saturated mudrocks based on in situ sonic and seismic measurements (Figure 5), given as:

$$Vp = 1.16Vs + 1.36 \qquad (13a)$$

or

$$Vs = .8621Vp - 1.1724 \qquad (13b)$$

where Vp and Vs are in kilometers per second. Examination of figure 5 gives an insight into the remarkable relationship, given that mudrocks are highly variable. One can see that the pure clay point lies very close to the line connecting the end members of pure water and pure quartz. As porosity of a pure clay increases, the velocities decrease in a linear manner towards that of pure water while as quartz is added to pure clay the velocities increase in a linear manner towards that of pure quartz (Castagna et al., 1985).

It was found that the mudrock line could further apply to water-saturated sandstones as Pickett's trend (Pickett, 1963) for sandstones based on laboratory measurements coincides precisely with the mudrock line. Laboratory measurements and data from the literature showed, in general, a good fit to the mudrock line (Figure 6).

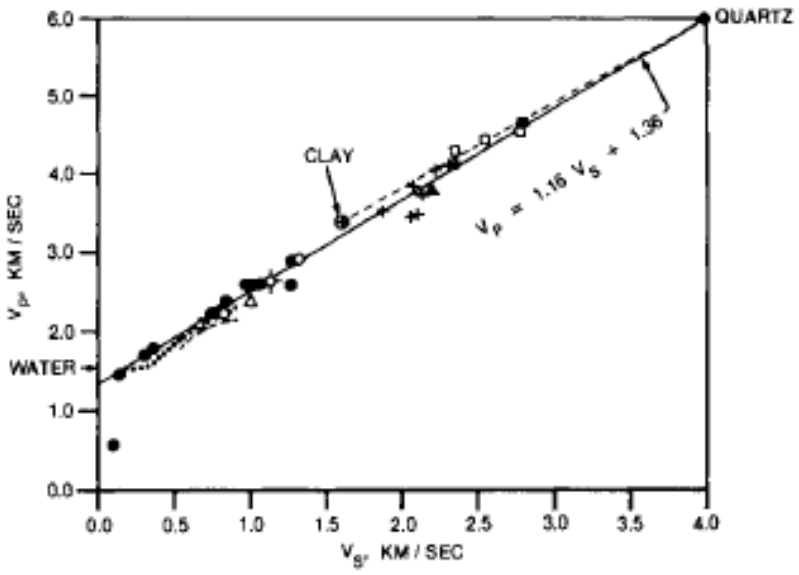

Figure 5: Empirical relationship between Vp and Vs found from in situ measurements at various formations. (Castagna et al., 1985)

The mudrock line has become a popular shear-wave velocity predictor that is easy to implement. However, its restriction to water-saturated sediments limits its effectiveness in hydrocarbon environments. Also, as an empirical formula, its accuracy at a given basin may be less than adequate depending on the objective.

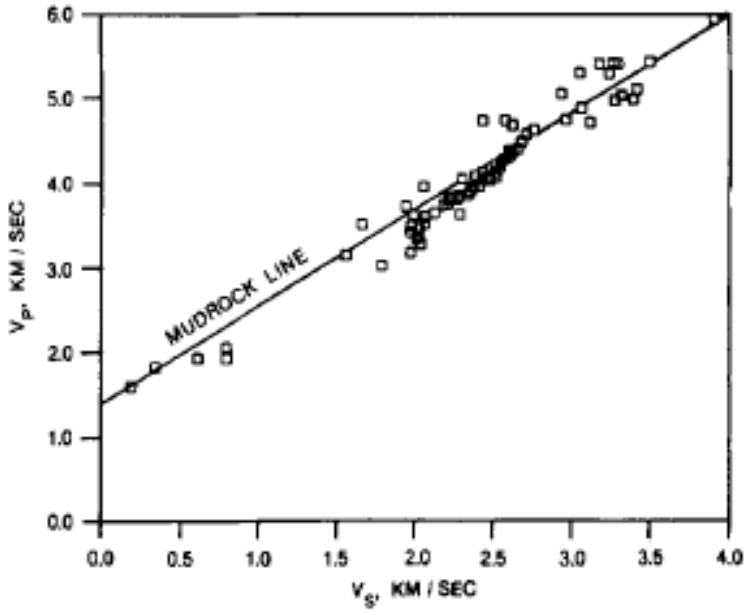

Figure 6: Compilation of Vp and Vs laboratory and literature data plotted with the mudrock line. (Castagna, 1985)

3.2.5 Greenberg-Castagna Empirical Formula

Greenberg and Castagna (1992) developed empirical relationships for estimating the shear-wave velocity of brine-saturated multiminerallic rocks based on empirical relationships of monominerallic rocks. Using these monominerallic velocity relationships, the shear-wave velocity of the composite can be calculated by an average of the harmonic and arithmetic means of the monominerallic shear-wave velocity, expressed as:

$$Vs\ (\frac{km}{s}) = \frac{1}{2}\left\{\left[\sum_{i=1}^{L} X_i \sum_{j=0}^{N_i} a_{ij}\, V^j p\right] + \left[\sum_{i=1}^{L} X_i (\sum_{j=0}^{N_i} a_{ij} V^j p)^{-1}\right]^{-1}\right\} \quad (14)$$

where L = the number of monomineralic constituents, X = the volume fraction of each constituent, a_{ij} = regression coefficients, N = the order of the regression polynomial, and Vp = the brine saturated, composite medium compressional velocity. Regression coefficients are given in table 1. The Greenberg-Castagna relations used in this study are those for a sandstone-shale system, expressed as:

$$Vs\left(\frac{km}{s}\right) = .8042Vp - .8559, \qquad for\ sandstones \quad (15a)$$

and

$$Vs\left(\frac{km}{s}\right) = .7700Vp - .8674, \qquad for\ shales \quad (15b)$$

	a	b	c
Limestone	-0.05508	1.01677	-1.03049
Dolomite	-	0.58321	-0.07775
Sandstone	-	**0.80416**	**-0.85588**
Shale	-	**0.76969**	**-0.86735**

Table 1: Vp-Vs regression coefficients for pure monomineralic rocks, from Castagna et al., (1993). Equation is of the form: $Vs = aVp^2 + bVp + c$

3.2.6 Non-Vp Regressions

Many other regression studies have been conducted to relate Vs to various properties, as has been done with the mudrock line and the GC equations in relation to Vp. To distinguish the following models from those, the equations in this section will be referred to as non-Vp regressions as they relate Vs to properties such as clay content and porosity, and not merely Vp. The non-Vp regressions discussed here can be found together in Castagna et al., (1993).

Tosaya (1982) related Vp and Vs to porosity and clay content through laboratory measurements of brine-saturated sandstones and shales at 5800 psi (40 MPa). Clay content was obtained by detailed chemical and petrographic analysis. The multiple regression of Vs to clay content and clay volume produced the equation:

$$Vs\left(\frac{km}{s}\right) = 5.8 - 8.6\varphi - 2.4X_{cl} \tag{16}$$

where φ = porosity and X_{cl} = fractional clay volume.

Castagna et al. (1985) followed a similar path of Tosaya (1982) and performed multiple linear regression of velocities versus porosity and clay content. However, their data was sonic log measurements from the Frio formation and clay content was determined by conventional log analysis. The resulting regression equation is:

$$Vs\left(\frac{km}{s}\right) = 3.89 - 7.07\varphi - 2.04X_{cl} \tag{17}$$

We can see the obvious resemblance to the Tosaya equation. The correlation coefficient of this equation on the Frio data was 0.96.

Han et al. (1986) conducted perhaps the most extensive study of velocities of clay-bearing sandstones. They measured the velocities of 75 sandstones in the laboratory at effective pressures ranging from 100 bars to 400 bars, porosities ranging from 2 to 30%, and clay volumes from 0 to 50%. Velocity regressions were done against clay volume and porosity for each pressure regime. The regression equation for Vs is:

$$Vs\left(\frac{km}{s}\right) = a + b\varphi - cX_{cl} \tag{18}$$

and the coefficients are given in table 2.

Eberhardt-Phillips et al. (1989) extended this study by adding effective pressure as a regression parameter and using nonlinear multiple regression. The resulting equation is:

$$Vs\left(\frac{km}{s}\right) = 3.70 + 4.94\varphi - 1.57\sqrt{X_{cl}} + .361(P - e^{-16.7P}) \tag{19}$$

where P is effective pressure in kilobars.

Effective pressure is defined as the difference between overburden (lithostatic) pressure and pore (hydrostatic) pressure. The equation for overburden pressure in Norne Field is (Dadashpour, 2009):

$$P_{OV} = 0.0981 * (9x10^{-5}TVD + 1.7252) * TVD \tag{20}$$

where TVD = true vertical depth. Pore pressure was calculated based on a formation pressure plot and results are in table. Subtracting the pressures given in table 3 from equation (20) provides the effective pressure for Norne Field.

Effective Pressure (Bars)	a	b	c
400	3.52	-4.91	-1.89
300	3.47	-4.84	-1.87
200	3.39	-4.73	-1.81
100	3.29	-4.73	-1.74

Table 2: Values of coefficients of equation 18 (Han regression). Taken from Castagna et al., (1993).

Depth Interval (m)	Initial Pressure (Bar)	Gradient (Bar/m)
2670-2709 (well #1) 2597-2638 (well #2)	290	0
2709-2792 (well #1) 2638-2738 (well #2)	245	0.0123
2792-2837 (well #1) 2738-2790 (well #2)	252.5	0.066

Table 3: Pore (hydrostatic) pressures in Norne Field.

3.2.7 Raymer-Hunt-Gardner (RHG) Vs Equation

Wyllie et al., (1956) developed a velocity-porosity transform by assuming that the wave propagates a fraction of its time in the matrix and a fraction of its time in fluid. The equation, known commonly as the Wyllie time-average equation, has no correct physics based derivation, but has been used over the years as an effective method of relating compressional velocity to porosity in well consolidated sandstones. Raymer et al., (1980) developed an improvement to the Wyllie equation, known as the Raymer-Hunt-Gardner (RHG) equation and is expressed as:

$$Vp = (1-\varphi)^2 Vp_{ma} + \emptyset V_f \quad (18)$$

where Vp_{ma} = the Vp in the matrix, φ = porosity, and Vp_f = the fluid velocity. Castagna (1985), using Biot-Gassmann theory, derived a Vs form of the RHG equation given as:

$$Vs = (1-\varphi)^2 Vs_{ma} \quad (19)$$

where Vs_{ma} = the Vs in the matrix. Dvorkin (2008) extended this equation by using the Gassmann assumption that the shear modulus is not affected by the pore fluid and developed the following RHG Vs equation for calculating the saturated Vs given that equation (19) represents dry Vs:

$$Vs = Vs_{dry}\sqrt{\frac{\rho_{dry}}{\rho_b}} = (1-\varphi)^2 Vs_{ma}\sqrt{\frac{(1-\varphi)\rho_s}{(1-\varphi)\rho_s + \varphi\rho_f}} \quad (20)$$

where ρ_{dry} = the bulk density of the dry sediment, ρ_b = the bulk density of the wet sediment, ρ_s = the density of the solid phase, ρ_f = the density of the fluid phase, and φ = porosity. It is obvious from the equation that the prediction is dependent on accurate estimates of densities and elastic moduli of the matrix, thus, the equation will provide a good test as to the accuracy of the inverted density and moduli values.

Chapter 4: Results for Well #1

The methods described in chapter 3 will now be used to predict the shear-wave velocity in well #1. An assumption is made that the lithologic environment is of two end members: sand and shale. No other local shear data or measurements are used in this part, thus this represents a blind prediction of shear-wave velocity based on compressional velocity and petrophysical log measurements.

4.1 Krief Model

The Krief model was used as described in section 3.2.1. K_{sand}, μ_{sand}, K_{shale}, and μ_{shale} were left as parameters to be solved by minimizing equation (8). As mentioned before, Vs has been removed from the objective function in order to use this method as a Vs predictor. The fluid properties (which can be left for the algorithm to solve) were solved beforehand based on the Batzle-Wang equations (Batzle and Wang, 1992). The input properties are given in table 4 and the output properties are given in table 5. An interval of 200 points in the Tofte formation (depth: 2740-2765 m) was used for the inversion as it is has the most uniform velocities and produced the best results. The moduli were constrained using upper and lower bounds so as to produce realistic results. The lower bounds are 25, 25, 10, and 1 for K_{sand}, μ_{sand}, K_{shale}, and $\mu_{shale,}$ respectively, while the corresponding upper bounds are 40, 45, 25, and 10. The resulting best fit elastic properties produced by the inversion are given in table 6. These shear moduli were then used to estimate Vs (Figure 7).

Brine Salinity (ppm)	Oil Gravity (API)	Gas Gravity (specific gravity)	Gas-Oil Ratio (L/L)	Pore Pressure (MPa)	Temperature (^{o}C)
50,000	32.7	0.85	111	27	100

Table 4: Input fluid properties for the Batzle-Wang equations.

Fluid	Density (g/cc)	Bulk Modulus (GPa)
Brine	1.0	2.7
Oil	0.73	0.65
Gas	0.24	0.07

Table 5: Output fluid properties of the Batzle-Wang equations.

K sand (GPa)	μ sand (GPa)	K shale (GPa)	μ shale (GPa)
39.8	30.6	13.4	8.3

Table 6: Elastic moduli inverted from Vp at well #1 using the Krief model.

We can see that solving for the elastic moduli over a small interval produces good results when applying those moduli to the entire log interval. The Vp estimation using the estimated moduli has a mean square error (MSE) of .1098 when compared to the measured Vp. Meanwhile, the predicted Vs has an MSE of .0557 when compared to the measured Vs, an excellent match considering no measured Vs values were used in the minimization. In fact, inverting Vs for shear moduli produced a u_{sand} = 31.2 and u_{shale} = 8.3. These results are very similar to those in table 6 and show the robustness of using Vp to predict Vs.

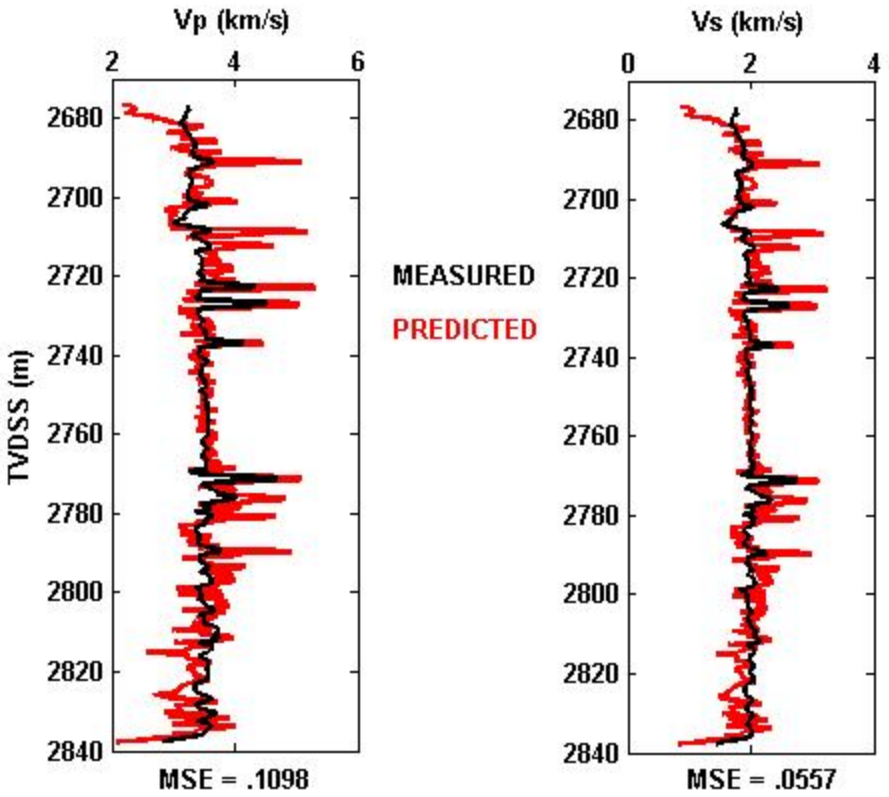

Figure 7: Velocity prediction at well #1 using the Krief method and inverting Vp for elastic moduli. Using the estimated moduli, the Vp estimation has an MSE = .1098 and the estimated Vs has an MSE = .0557.

Comparing the Vs estimation error to the measured logs shows a slight correlation between Vp, density, and porosity (Figure 8). Several of the large Vs errors can be linked to high Vp, high density, and high porosity. This is likely a lithology effect due to dense, tight streaks such as limestone or cemented sand. There appears to be no correlation between the Vs error and shale volume, indicating that the inversion has successfully inverted for both sand and shale properties.

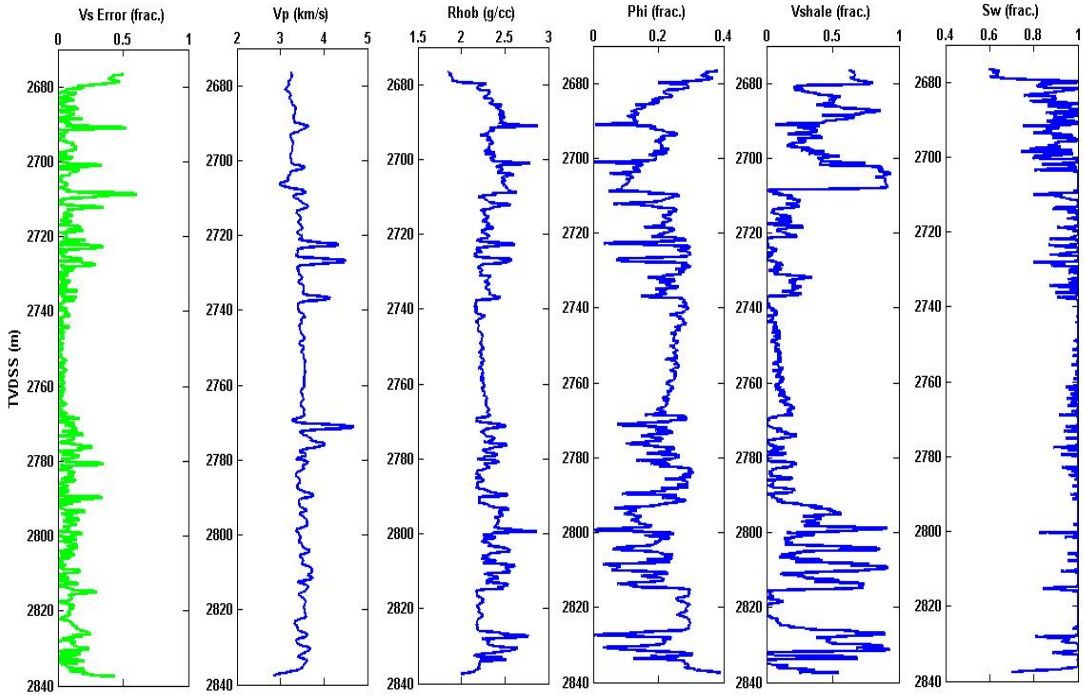

Figure 8: Comparison of Krief-predicted Vs error (left column) at well #1 with the measured logs. There exists a slight correlation between the error and Vp, density, and porosity. Several of the higher error data points are tracked to points of high Vp, high density, and low porosity.

If we look at the Vp/Vs ratio for this well, we see that most of the clean sands lie between ratios of 1.7 to 1.8, while the shaley units have Vp/Vs ratios greater than 1.8 (Figure 9). The Krief-predicted Vs does not adequately allow for this distinction between the lithologies. We see a much higher variation in Vp/Vs ratios for the sands and an overlap of the sand and shale ratios.

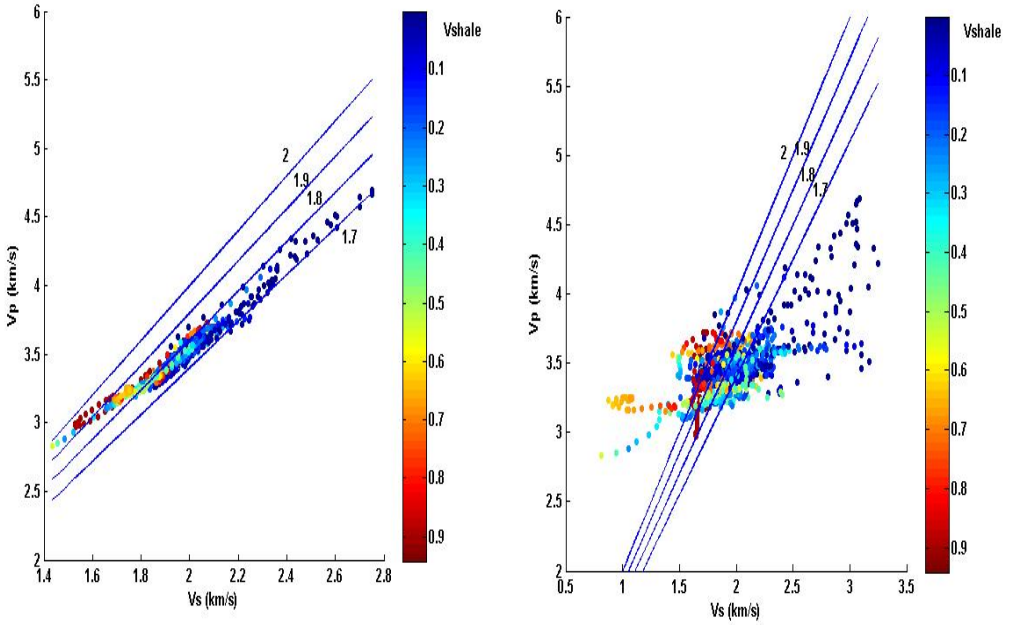

Figure 9: Measured Vp vs. measured Vs (left) compared with measured Vp vs. Krief-predicted Vs (right) at well #1. Data is color coded by shale volume. The measured data shows sands having Vp/Vs ratios ranging from 1.7-1.8 while the shaley units have Vp/Vs ratios greater than 1.8. Using the Krief-predicted Vs does not provide the same level of lithology distinction.

4.2 Self-consistent (SC) Method

The self-consistent effective medium method was described in section 3.2.2. Along with inverting for the elastic moduli, the aspect ratios of the sand/shale grains and sand/shale porosities were also left as free parameters to be solved by the genetic algorithm. The aspect ratios of the sand grains were constrained with a lower bound of .1

and an upper bound of .99 while the bounds for the shale grains were .01 and .99, respectively. The aspect ratio of the sand porosity was constrained with a lower bound of .01 and an upper bound of .3 while the bounds for the shale porosity are .001 and .1, respectively. The Vp-inverted, best fit aspect ratios are given in table 7.

These shear moduli and aspect ratios were then used in the SC model to predict Vs (Figure 10). The MSE for Vp prediction is .0795 while it is .0568 for Vs prediction. Based on the MSE, we see nearly identical results to the Vs prediction using the Krief model, however, visual inspection shows that the SC inversion slightly overestimates the shear velocity for the clean sand interval. Comparison of the elastic moduli provides evidence that the sand grain/porosity aspect ratios may be too high. The sand bulk modulus of 30.5 inverted using the SC method is much lower than the 39.8 inverted using the Krief model, however, the Vp prediction in the clean interval is similar for both models. It is likely that the algorithm produced higher aspect ratios to compensate for the lower bulk modulus in order to provide the best match to the velocities. Also, the inverted sand shear modulus using the SC model is slightly lower than that using the Krief model which obviously wouldn't explain an overprediction of velocity.

	K	μ	Aspect Ratio
Sand grains	30.5	28.6	.193
Shale grains	21.2	9.9	.054
Sand porosity	-	-	.245
Shale porosity	-	-	.1

Table 7: Inverted moduli and aspect ratios from Vp inversion at well #1 using the SC method.

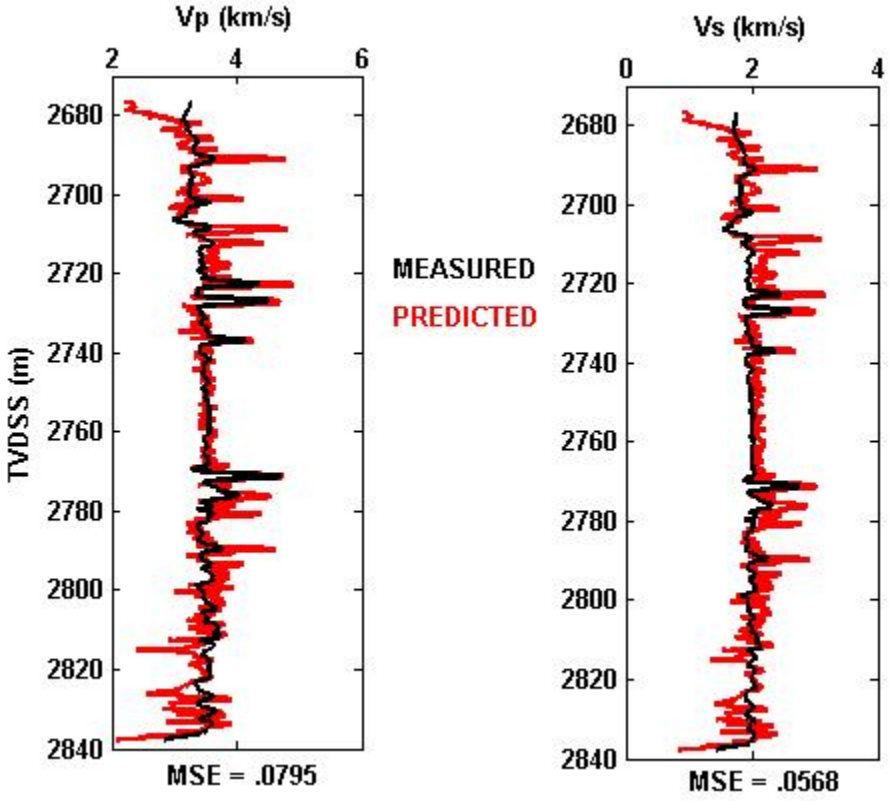

Figure 10: Velocity prediction results at well #1 using the inverted moduli and aspect ratios in the self-consistent method. The MSE = .0795 and .0568 for Vp and Vs estimation, respectively.

Comparison of the prediction error with the measured logs shows a correlation with density and porosity (Figure 11). The points of largest error coincide with the points of high density and low porosity. Once again, it can be reasoned that this is a lithology effect due to tight streaks.

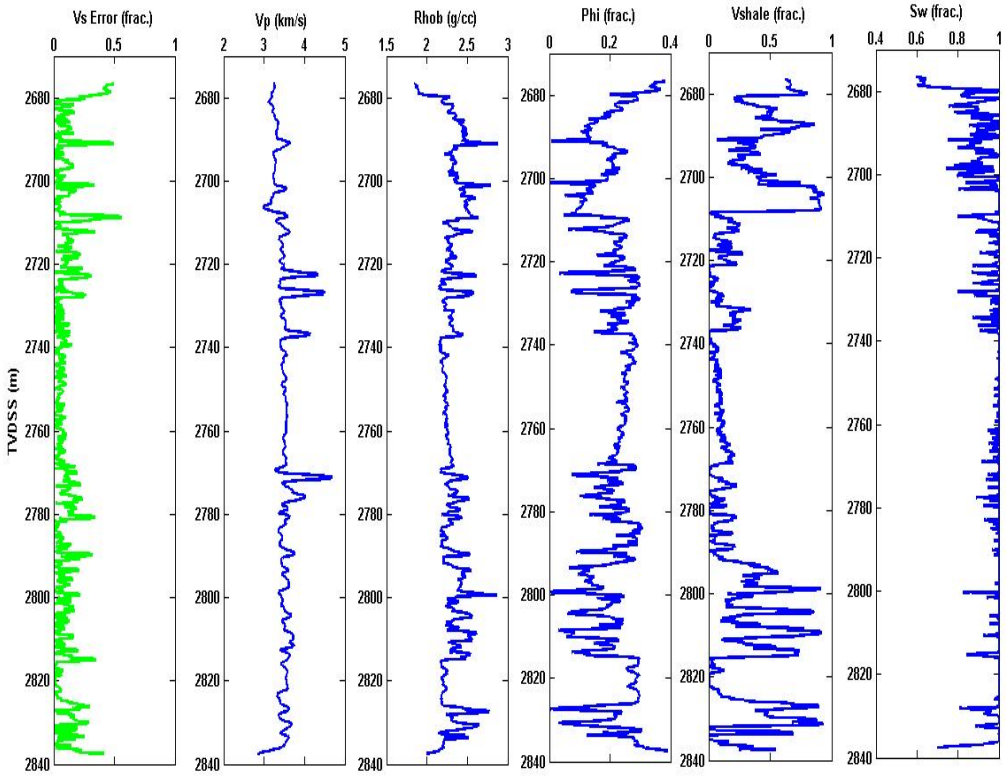

Figure 11: Comparison of the SC-predicted Vs error (left column) at well #1 with the measured logs. We see a correlation between the Vs error and density and porosity. Many of the large error points coincide with high density and low porosity.

Lithology distinction using the SC-predicted Vs is slightly better than what we saw using the Krief-predicted Vs (Figure 12). The shaliest units have Vp/Vs ratios of

greater than 2 and are clearly separated from the sandstones, however, the moderately shaley points with Vp/Vs ratios ranging from 1.7-2 overlap with much of the sand data points. We begin to separation with the cleanest sandstones having low Vp/Vs ratios, below 1.7.

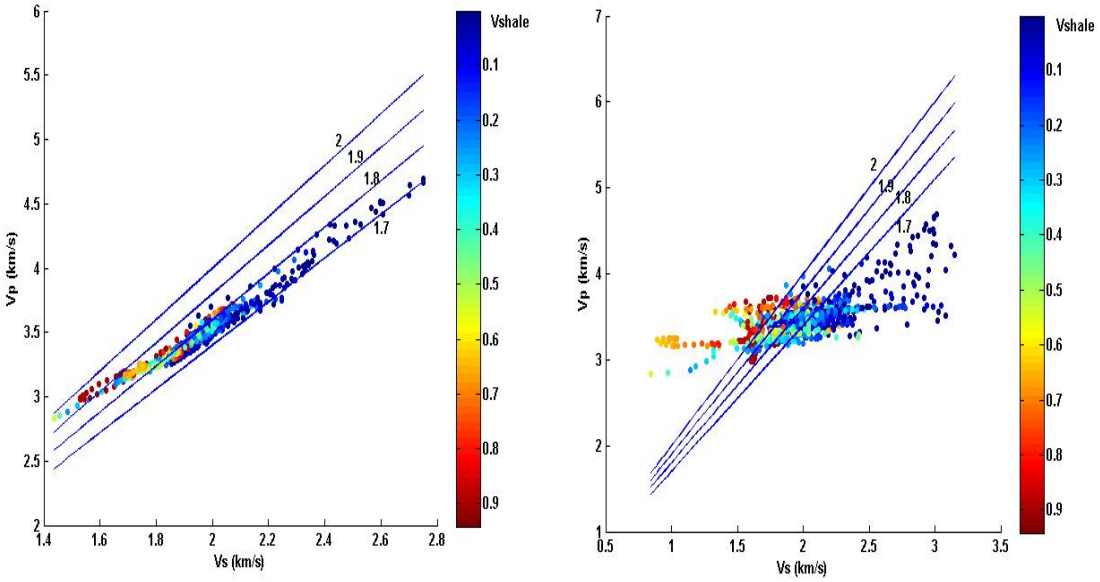

Figure 12: Measured Vp vs. measured Vs (left) compared with measured Vp vs. SC-predicted Vs (right) at well #1. The shaliest and cleanest units can be detected by the Vp/Vs ratios using the SC-predicted Vs.

4.3 DEM Method

The DEM method was described in section 3.2.3. While the SC method involves the grain aspect ratios, the DEM method only involves aspects ratios of the porosities and thus these two parameters were left to be solved by the genetic algorithm, along with the elastic moduli. The same constraints that were previously used were used in the DEM inversion. The results of inverting Vp for the elastic moduli and sand/shale aspect ratios are given in table 8.

These moduli and aspect ratios were then used in the DEM method to predict Vs (Figure 13). The MSE for Vp prediction is .1139 while for Vs prediction it is .1071. We see that the prediction using the DEM at this well is not as accurate as the Krief or SC method. Interestingly, the shear moduli and sand/shale porosity aspect ratios are lower than those inverted from the SC method, yet Vs is slightly overpredicted using the DEM method.

	K	**μ**	**Aspect Ratio**
Sand grains	26.1	26	-
Shale grains	24.9	10	-
Sand porosity	-	-	.04
Shale porosity	-	-	.012

Table 8: Elastic moduli and aspect ratios from Vp inversion at well #1 using the DEM method.

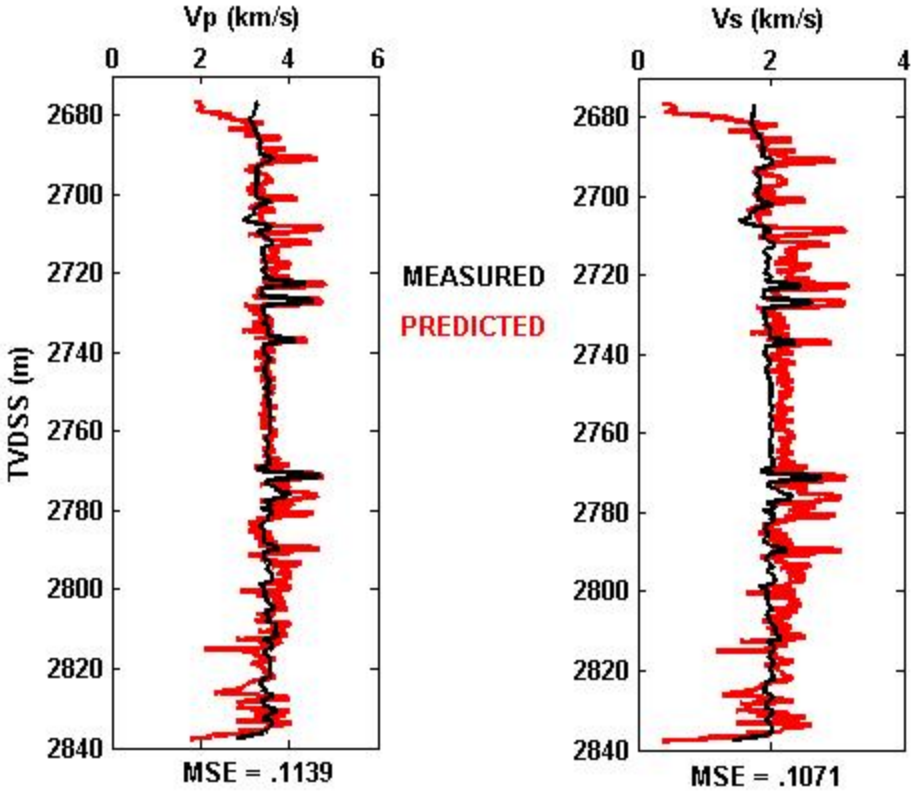

Figure 13: Velocity prediction results at well #1 using the DEM method. MSE for Vp prediction is .1139 and .1071 for Vs prediction.

The predicted error shows a strong correlation with density (Figure 14). The error follows a similar trend to the density trend, with much of the higher error correlating with higher density. In turn, the higher error can also be correlated with lower porosity.

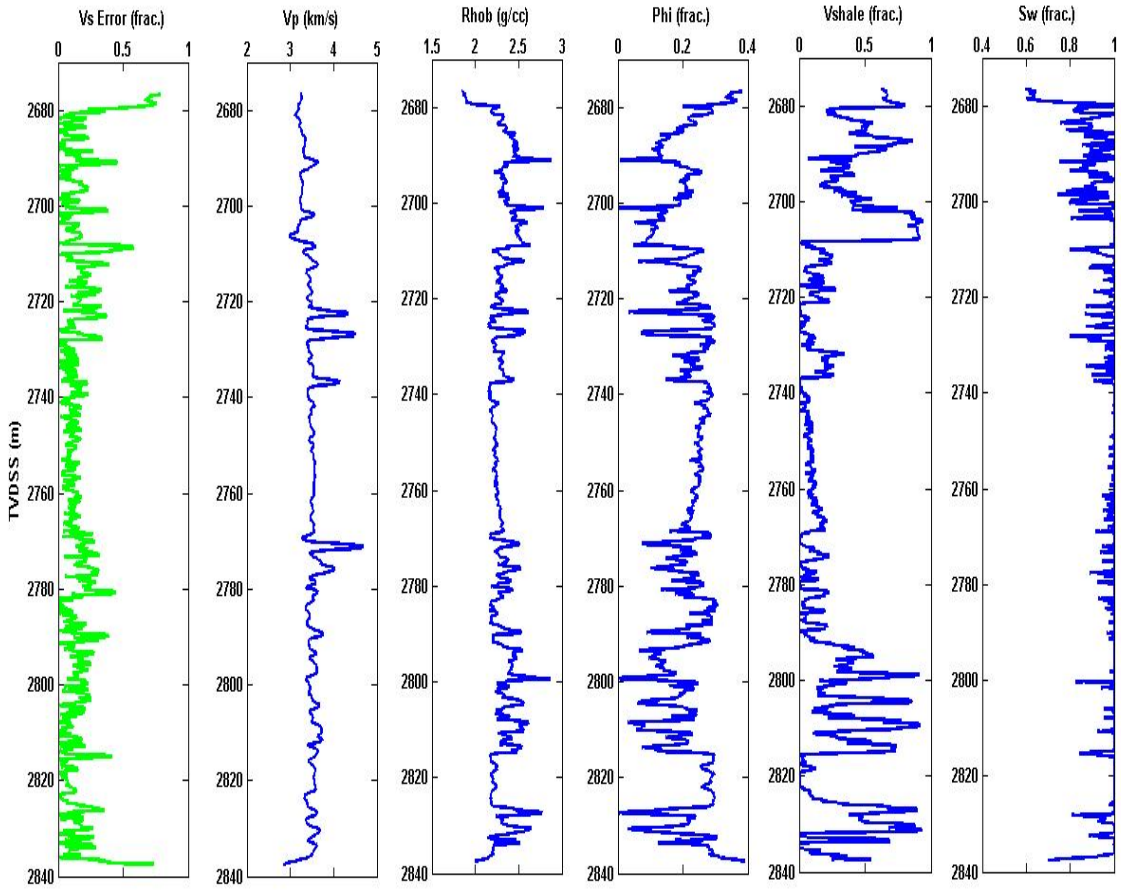

Figure 14: Comparison of the DEM-predicted Vs error with the measured logs at well #1. A correlation exists between the error, density, and porosity. Higher density, coinciding with lower porosity, tends to increase the predicted error.

Lithology identification using the DEM-predicted Vs is the least accurate of the three methods used in the inversion scheme (Figure 15). We see a wide range of Vp/Vs ratios with many pure shale data points showing similar ratios to clean sand points. The overprediction of Vs for both sandstone and shale leads to lower Vp/Vs ratios, and thus less lithology distinction.

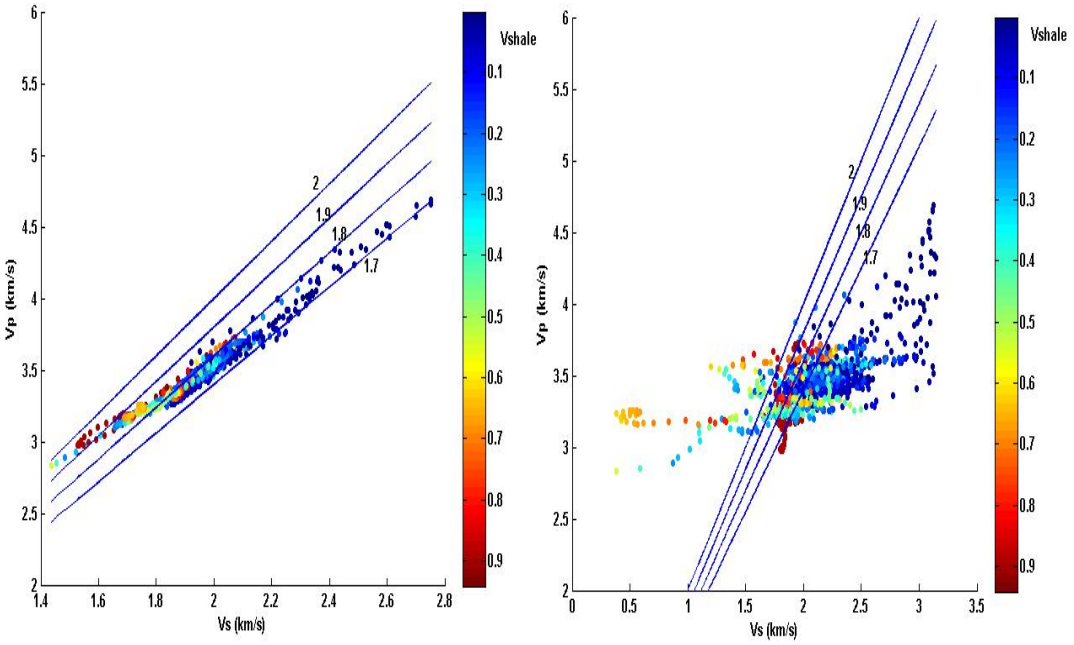

Figure 15: Measured Vp vs. measured Vs (left) compared with measured Vp vs. DEM-predicted Vs at well #1. Lithology identification is mostly ambiguous using this Vs.

4.4 The Mudrock Line

Figure 16 shows the results of Vs prediction using the mudrock line. The MSE is .0194. We can see that the mudrock line produces a good trend to the measured Vs but under-predicts the velocity, which results in a higher Vp/Vs ratio than what is given by the measured values (Figure 17). It is possible that this discrepancy is due to the pore geometry. As explained in Castagna et al., (1985), we would expect a formation with

equant pores to have a lower Vp/Vs ratio and data would lie above the mudrock line, as we see in figure 17. This also may lead to the conclusion that the self-consistent inverted aspect ratios, as opposed to the DEM results, are more representative of the actual conditions. Thin section data would be needed for further proof of the pore geometry effect on the mismatch of the mudrock line.

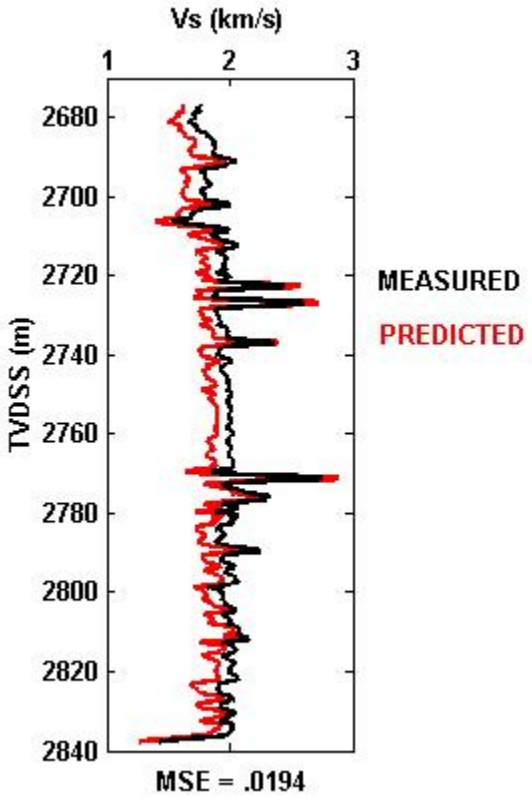

Figure 16: Results of Vs prediction at well #1 using the mudrock line. MSE is .0194.

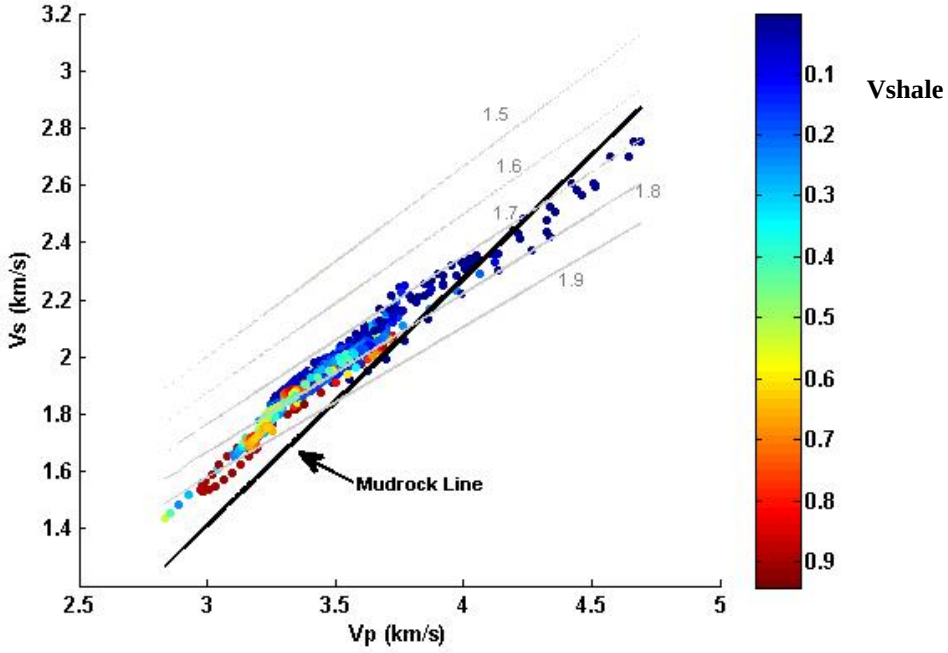

Figure 17: Vs vs. Vp for well #1. The mudrock line, as well as constant Vp/Vs ratio lines, is plotted with the measured data. The data is color-coded by shale volume.

4.5 Greenberg-Castagna Empirical Formula

The GC prediction was used with equations (15a) and (15b) for sand and shale, respectively, with the coefficients provided in table 9. The resulting prediction is shown in figure 18. We can see the excellent prediction that the GC formula provides, with a MSE of .0044. This is a better match than any of the previous models and shows the effectiveness of this method in brine-saturated sand/shale environment.

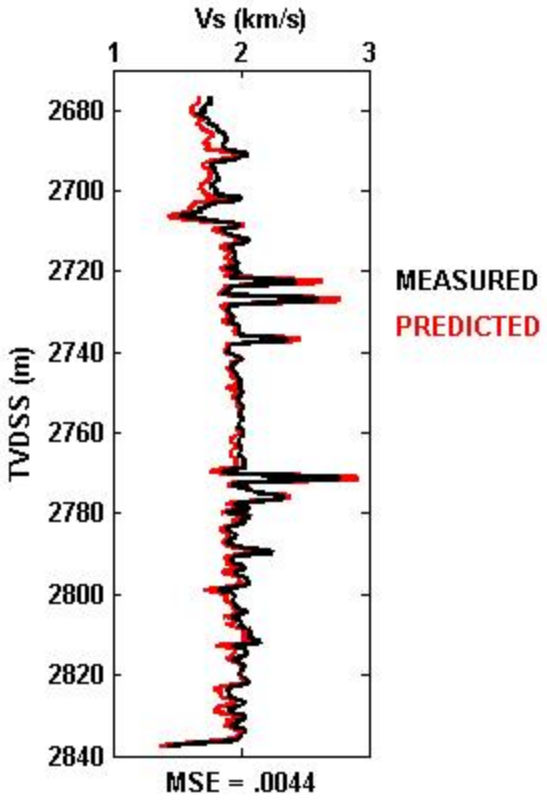

Figure 18: Vs prediction at well #1 using the Greenberg-Castagna empirical formulas. The MSE is .0044.

4.6 Non-Vp Regression Equations

Equations (16), (17), (18), and (19) were tested against the measured Vs using the coefficients provided in the respective tables in section 3.2.6. Results are shown in figure 19. We see that each regression equation provides a reasonably accurate prediction to the measured Vs. Based on the MSE the Han regression provides the best estimate with an MSE of .0960, followed by the Eberhardt-Phillips regression (.1067), the Tosaya regression (.1305), and the Castagna regression (.1700). However, if we focus on the clean sand interval with a uniform Vs, we see that the Tosaya regression is the most

accurate, while the Han and Eberhardt-Phillips regressions slightly overestimate Vs and the Castagna regression slightly underestimates Vs.

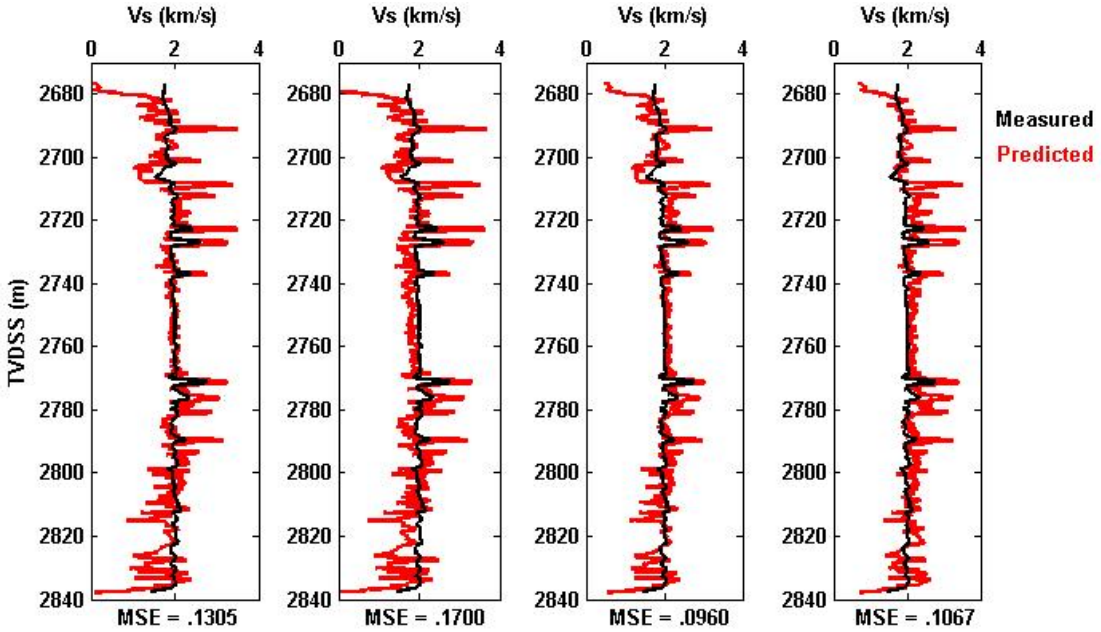

Figure 19: Vs prediction for well #1 using the non-Vp regression equations. The predictions from left to right are based on equations (16), (17), (18), and (19). Equations and coefficients are given in section 3.2.6.

4.7 Raymer-Hunt-Gardner (RHG) Vs Equation

The Raymer-Hunt-Gardner Vs equation was described in section 3.2.7. The inverted sand and shale densities as shown in figure 4 and shear moduli inverted by the Krief model were used in equation (20). The matrix shear modulus was determined by VRH averaging and this modulus was used to find the matrix shear velocity. Vs for well #1 was then predicted using equation (20). The resulting prediction is shown in figure 20.

We see that the RHG Vs model provides a good match to the measured Vs with an MSE of .0462. As this model is dependent on the shear moduli and densities used, we see that the moduli and densities inverted using the genetic algorithm with the Krief model are proper values to be used at this well.

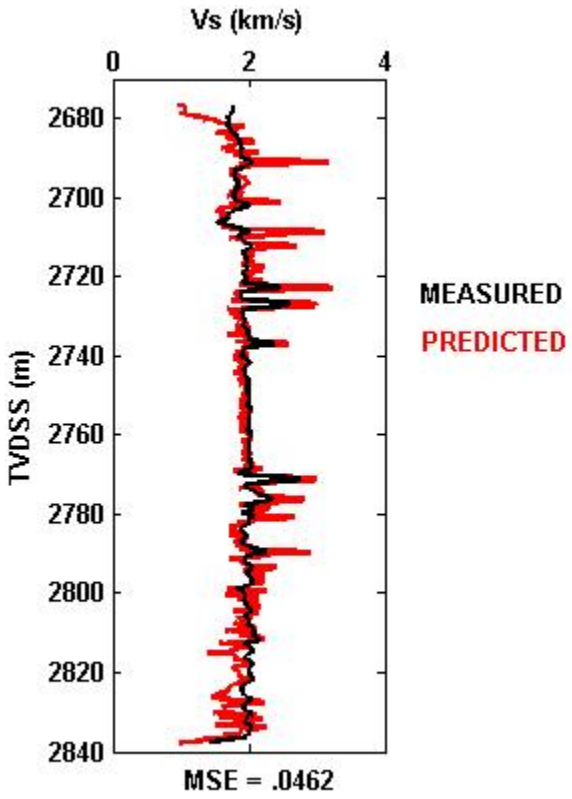

Figure 20: Vs prediction results for well #1 using the RHG Vs equation. The MSE is .0462.

4.8 Summary

A summary of the Vs prediction results are provided in table 9. The correlation coefficient (R^2) was also calculated for each prediction to show the pitfalls of such an error measurement. R^2 is arguably the most widely used error measurement but we can see from this study that it can give misleading results. If we guided our results by R^2, we

would assume that the mudrock line would be an optimal method to use. However, we saw from comparison to the measured Vs that the mudrock prediction underpredicts the velocity and we'll see in a later chapter that it has a strong effect on AVO modeling.

Model	Mean Squared Error (MSE)	Correlation Coefficient (R^2)
Krief	**.0557**	**.4961**
Self-consistent (SC)	**.0568**	**.5057**
DEM	**.1071**	**.4630**
Mudrock Line	**.0194**	**.9570**
Greenberg-Castagna (GC)	**.0044**	**.9572**
Tosaya Regression	**.1305**	**.4784**
Castagna Regression	**.1700**	**.4676**
Han Regression	**.0960**	**.4657**
Eberhardt-Phillips Regression	**.1067**	**.5120**
RHG	**.0462**	**.5065**

Table 9: MSE and correlation coefficient results for the Vs prediction models at well #1

Chapter 5: Results for Well #2

The next objective was to predict Vs at well #2. Where applicable, it is assumed that shear data for well #1 are available and can be used for better prediction at well #2. Aside from the predictions derived from well #1 data, the same methods used to predict Vs at well #1 have been used.

5.1 Krief Method

In the same manner as well #1, Vp at well #2 was inverted for the elastic moduli using the Krief model given by equation (8). A 200 point, clean interval (depth: 2677-2700 m) was used for the inversion. The same constraints for the moduli used at well #1 were applied here. The best fit elastic moduli are given in table 10. These shear moduli were then used to predict Vs. We see that the sand and shale shear moduli inverted as this well are higher than those from well #1, which were 30.6 and 8.3, respectively.

K sand (GPa)	μ sand (GPa)	K shale (GPa)	μ shale (GPa)
37.9	39.2	24.9	10

Table 10: Elastic moduli inverted from well #2 using the Krief model.

These shear moduli were then used to predict Vs (Figure 21). The prediction is less accurate than that at well #1, with an MSE of .1203 compared to that of 0.557 at well #1. From figure 21, we can see that Vs is overpredicted for much of the interval, bringing

into question the larger shear moduli at this well. However, inverting Vs alone for the shear moduli produced only a slightly lower μ_{sand} of 37.4 and the same μ_{shale} of 10.

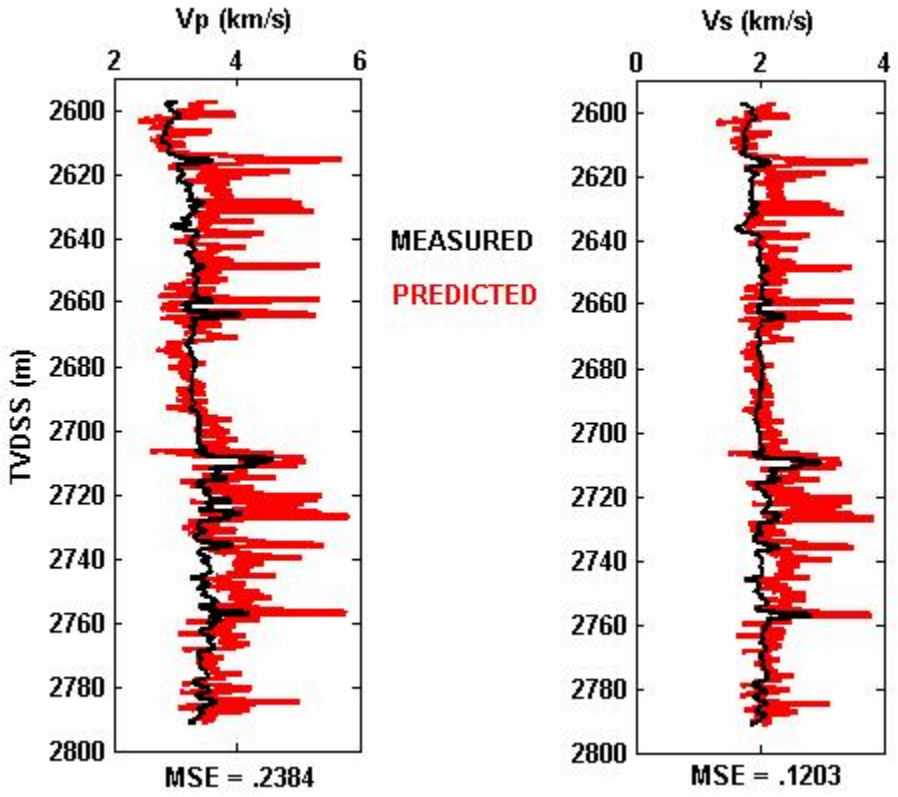

Figure 21: Velocity prediction results at well #2 using the elastic moduli inverted from Vp using the Krief model. The MSE for Vp prediction is .2384 while for Vs it is .1203.

The predicted Vs error shows a strong correlation with Vp, density, and porosity (Figure 22). The error trend closely follows the density trend, with higher error coinciding with higher density, which in turn coincides with lower porosity. Also, we see that points of higher Vp tend to produce greater error in the Vs prediction.

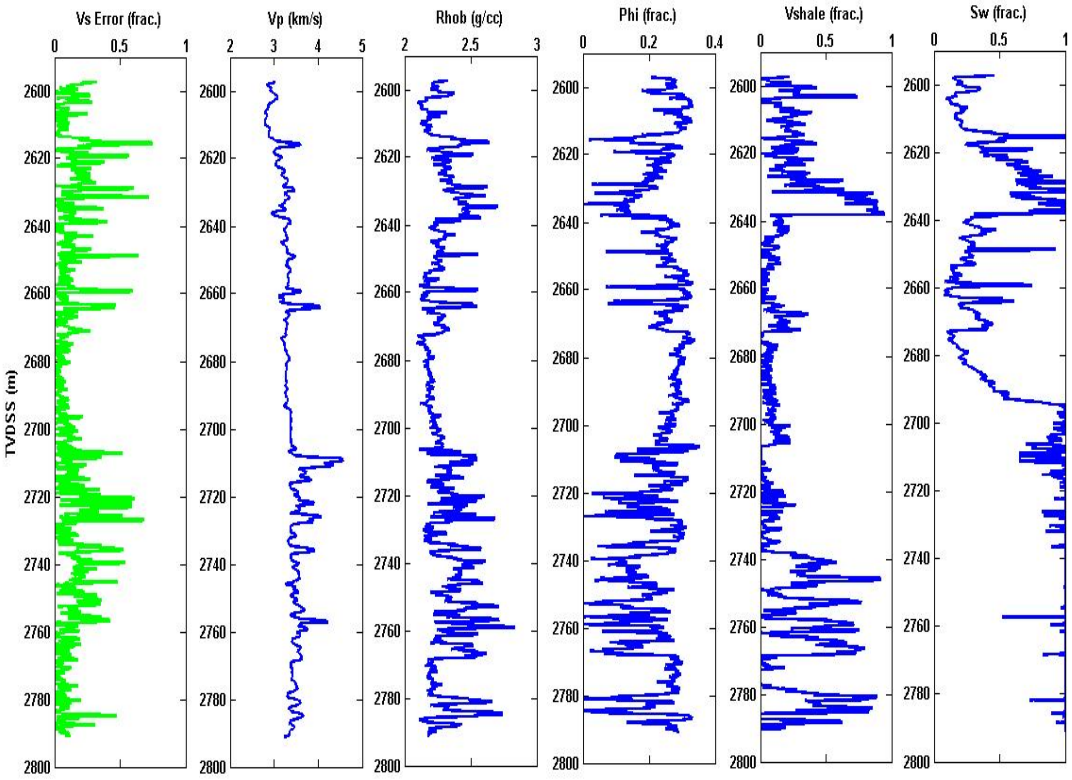

Figure 22: Comparison of the Vs error using the Krief model (left column) with the measured logs at well #2. We see the best correlation with Vp, density, and porosity. Much of the higher error correlates with higher Vp, higher density, and lower porosity.

The Vp/Vs ratios at this well are lower than those at well #1, with the shaliest points having ratios between 1.8 and 1.9 and a majority of the cleanest sand points lying between 1.6 and 1.7 (Figure 23). The Krief-predicted Vs provides a poor lithology distinction using Vp/Vs. We seem almost complete ambiguity between the shales and clean sandstones.

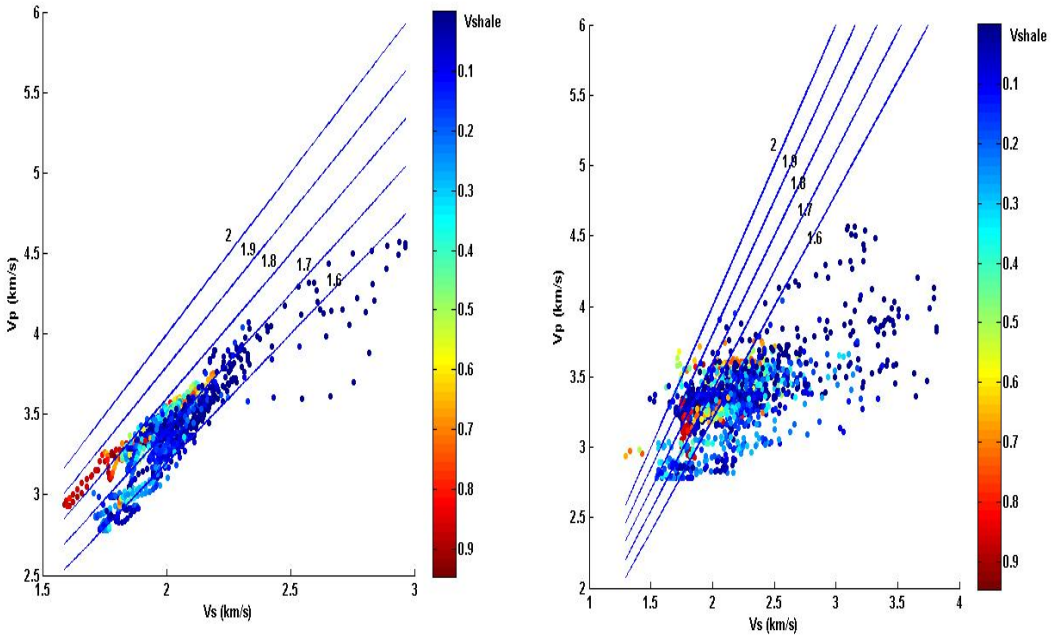

Figure 23: Measured Vp vs. measured Vs (left) compared with measured Vp vs. Krief-predicted Vs at well #2. Using the predicted Vs, we are unable to distinguish the shales from the sands using Vp/Vs.

5.2 Self-consistent (SC) Method

Using the same constraints for the elastic moduli and aspect ratios at well #1, Vp at well #2 was inverted using the SC model to solve for the parameters. The inverted, best fit moduli and aspect ratios are given in table 11. These parameters were then used in the SC model to predict Vs (Figure 24).

We see a much better Vs prediction using the SC method at this well than the prediction using the Krief model. The MSE for Vp prediction is .0821 while it is .0632

for Vs prediction. However, we still see a slight overprediction of Vs for most of the log interval. As the sand shear modulus inverted using the SC method is much lower than that inverted from the Krief model, the inverted sand geometry parameters must account for the overprediction. As we saw with well #1, the inverted sand porosity is atypically large and may account for the velocity mismatch. Nevertheless, we see that the SC method is much more effective at predicting Vs at well #2 than the Krief model.

	K	**μ**	**Aspect Ratio**
Sand grains	25.9	29.9	.107
Shale grains	25	10	.032
Sand porosity	-	-	.261
Shale porosity	-	-	.1

Table 11: Elastic moduli and aspect ratios inverted from Vp at well #2 using the SC method.

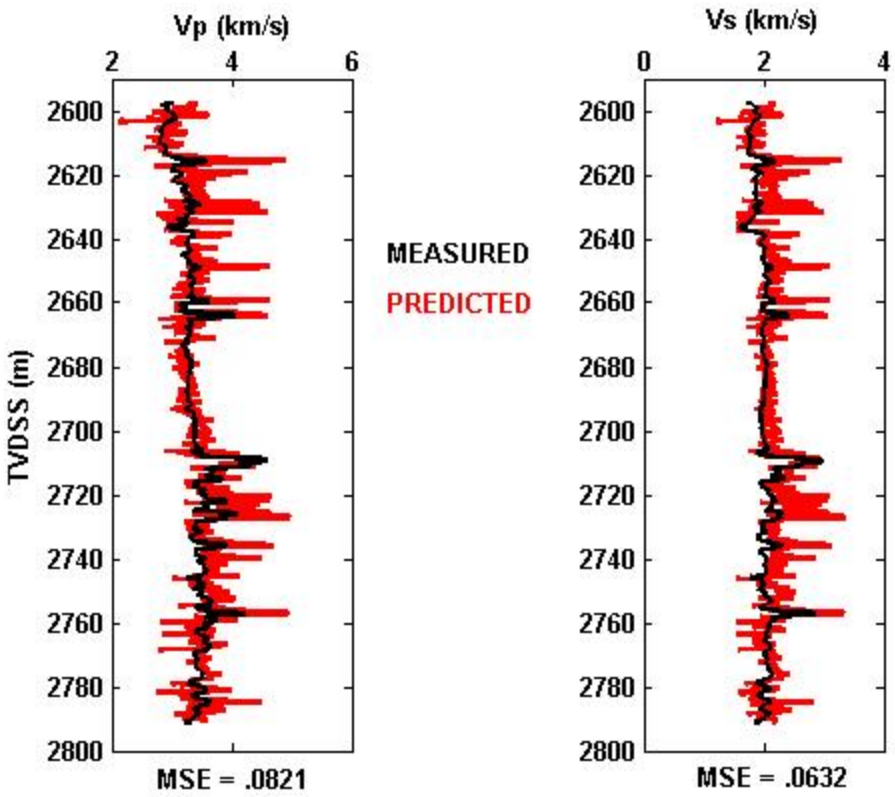

Figure 24: Velocity prediction results at well #2 using the elastic moduli and aspect ratios inverted from Vp using the SC method. The MSE for Vp prediction is .0821 and .0632 for Vs prediction.

As we have seen previously, we continue to see a correlation between the predicted Vs error and Vp, density, and porosity (Figure 25). The strongest correlation exists between the error and density with the highest errors being associated with the highest densities. Spikes in error can also be seen to correlate with high spikes in Vp and low spikes in porosity.

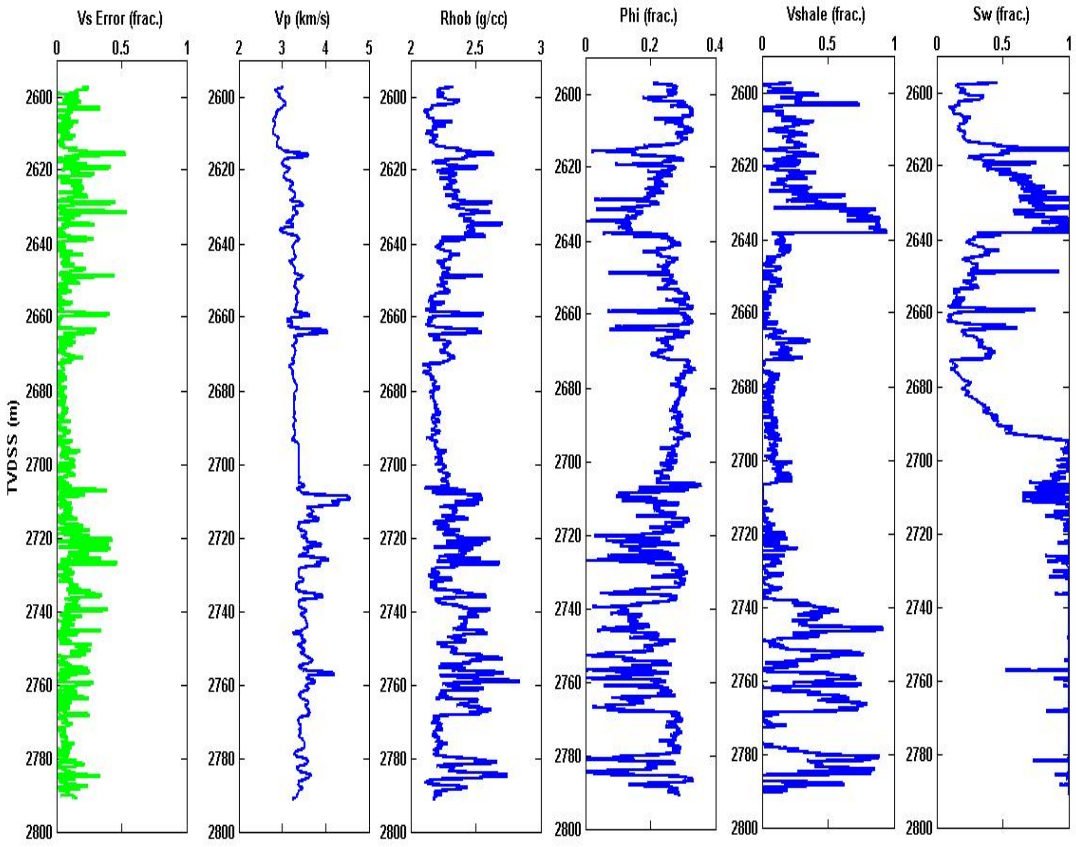

Figure 25: SC-predicted Vs error (left column) compared with the measured logs at well #2. The larger errors tend to coincide with higher Vp, higher density, and lower porosity.

The SC-predicted Vs at this well does a better job of delineating lithology using Vp/Vs than did the Krief method (Figure 26). The shale Vp/Vs ratios are higher than the actual measured values while the sand ratios are lowered than measured and thus we see a noticeable distinction between the shaley and clean units. The moderately shaley points still retain their ambiguity that is present in the measured case.

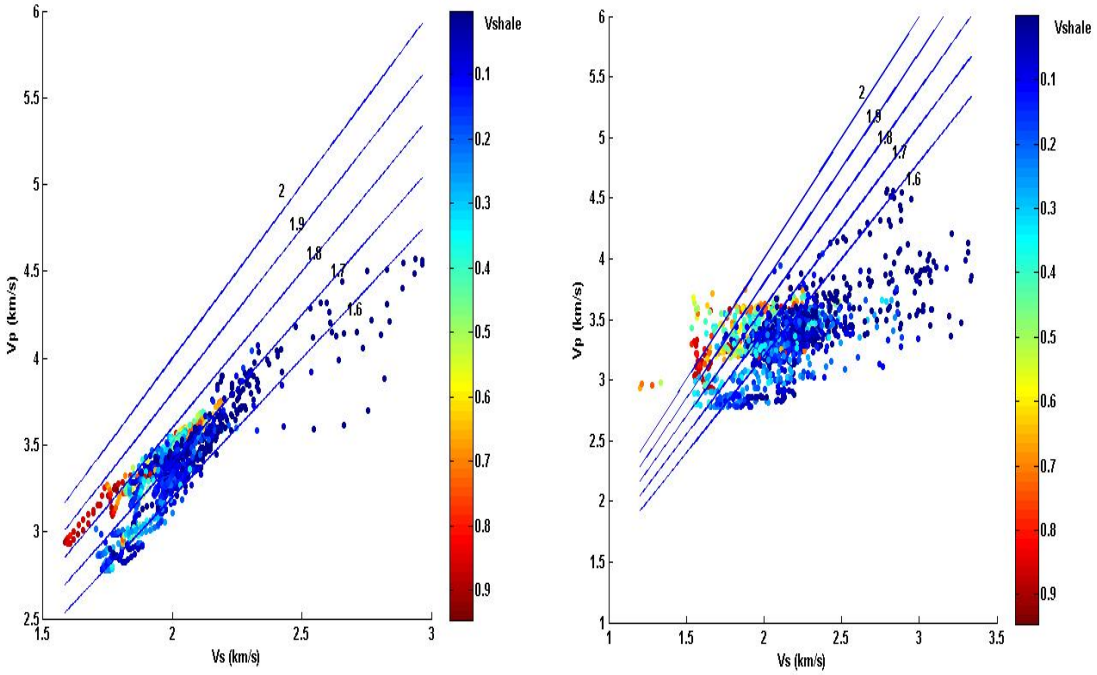

Figure 26: Measured Vp vs. measured Vs (left) compared with measured Vp vs. SC-predicted Vs (right) at well #2. We see different Vp/Vs ratios then given by the measured values but there is a visible distinction between the shaliest points and the cleanest points.

5.3 DEM Method

The Vp inverted elastic moduli and sand/shale porosity aspect ratios at well #2 using the DEM method are given in table 12. These shear moduli and aspect ratios were then used in the DEM method to predict Vs (Figure 27). The MSE for Vp prediction is .1016 and .0883 for Vs prediction. Once again, the Vs prediction is not as good as that provided by the SC method. However, the MSE at well #2 using the DEM method is

actually lower than that of well #1. Vs is overpredicted despite the lower shear moduli values as compared to the other models, similar to what we saw at well #1. Also, we see that the inverted shale porosity aspect ratio is larger than the sand porosity aspect ratio. A geometric regime of this manner is highly unlikely, however, thin section analysis would be needed as verification.

	K	**μ**	**Aspect Ratio**
Sand grains	25	26.1	-
Shale grains	19.4	5	-
Sand porosity	-	-	.042
Shale porosity	-	-	.099

Table 12: Elastic moduli and aspect ratios inverted from Vp at well #2 using the DEM method.

The prediction error follows the same trend as seen in the other models. The largest errors can be correlated to higher density and lower porosity (Figure 28). To a lesser extent, there is correlation between the error and Vp with several of the high jumps in error being associated with high jumps in Vp.

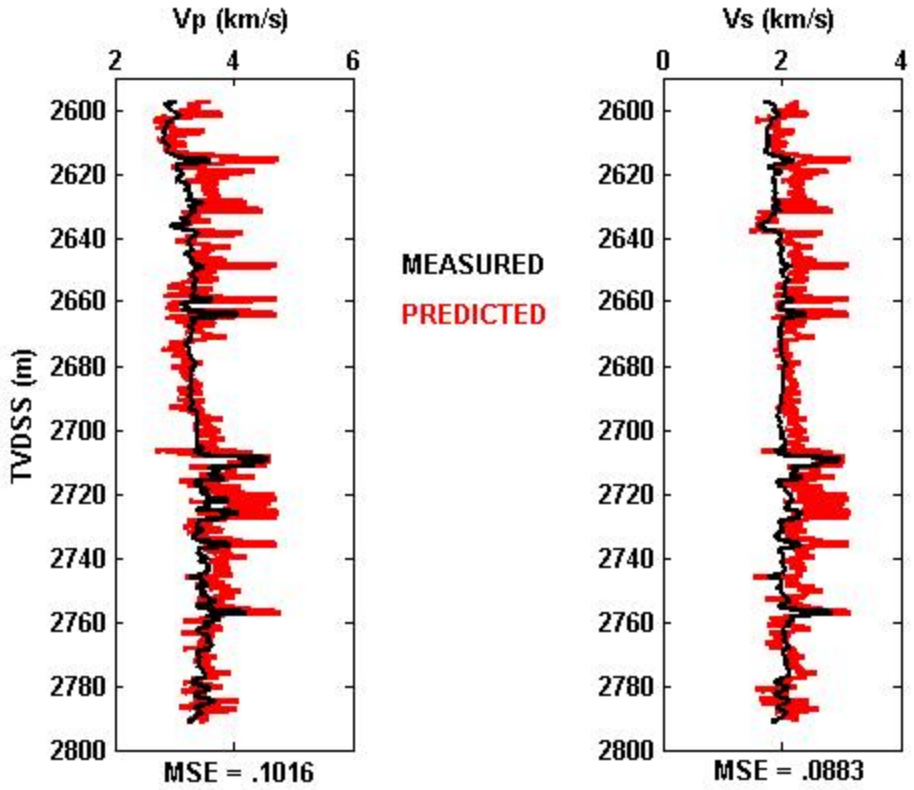

Figure 27: Velocity prediction results at well #2 using the Vp-inverted elastic moduli from the DEM method. MSE for Vp = .1016 and .0883 for Vs.

The Vp/Vs ratios of the shaliest units using the DEM-predicted Vs are larger than what is given by the measured values, while the cleaner sand Vp/Vs are smaller than those of the measured values (Figure 29). Hence, we are able to distinguish between sand and shale using Vp/Vs with the DEM-predicted Vs.

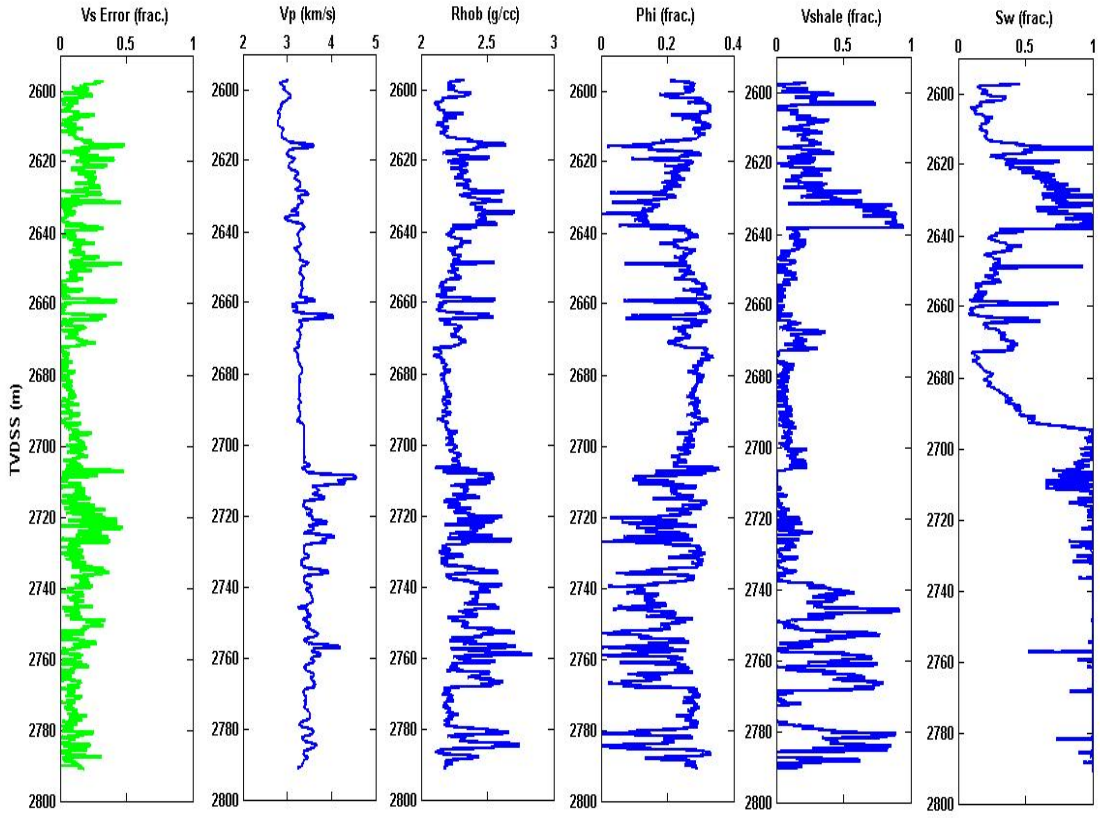

Figure 28: DEM-predicted Vs error (left column) compared with the measured logs at well #2. There is a noticeable correlation between the error, density, porosity, and to a lesser extent, Vp. Higher error correlates with higher density and lower porosity. Several of the largest errors can also be attributed to high Vp values.

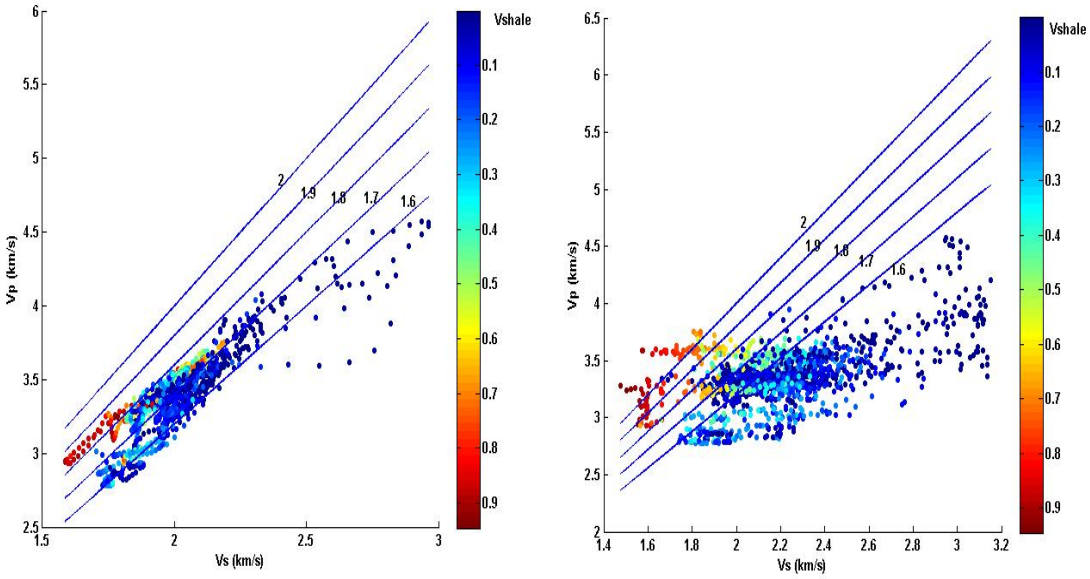

Figure 29: Measured Vp vs. measured Vs (left) compared with measured Vp and DEM-predicted Vs. There is visible distinction between the shaliest points and the clean points.

5.4 The Mudrock Line

The mudrock line is applicable only to water-saturated sediments and thus well #2 was first fluid substituted using Gassmann's equation to full water saturation. The elastic moduli used for the fluid substitution are those inverted from the Krief model and the dry frame bulk modulus was represented by the Krief model, equation (10a). The mudrock line was then used to predict Vs (Figure 30). The MSE at well #2 using the mudrock line is .0378, higher than that at well #1 which was .0194. This is expected as errors in fluid substitution are propagated into the Vs prediction. Similar to well #1, the mudrock line underpredicts Vs for most of the well.

Using the assumption that well #1 Vs data exists, a local mudrock trend was derived (Figure 31). The best-fit regression to Vp and Vs at well #1 is:

$$Vs\left(\frac{km}{s}\right) = .684Vp - .421 \qquad (21)$$

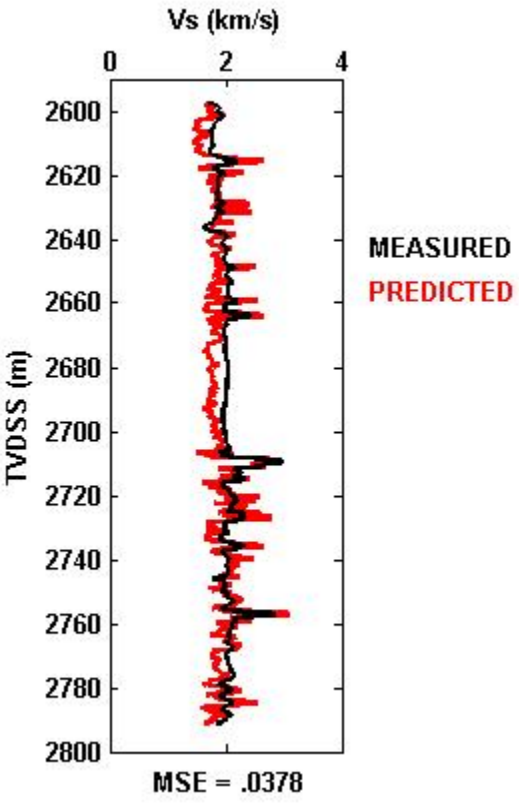

Figure 30: Vs prediction at well #2 using the mudrock line. The MSE is .0378.

Using this equation to predict Vs at well #2 produces a better fit, with an MSE of .0162 (Figure 32). This prediction is also slightly better than the mudrock prediction at well #1.

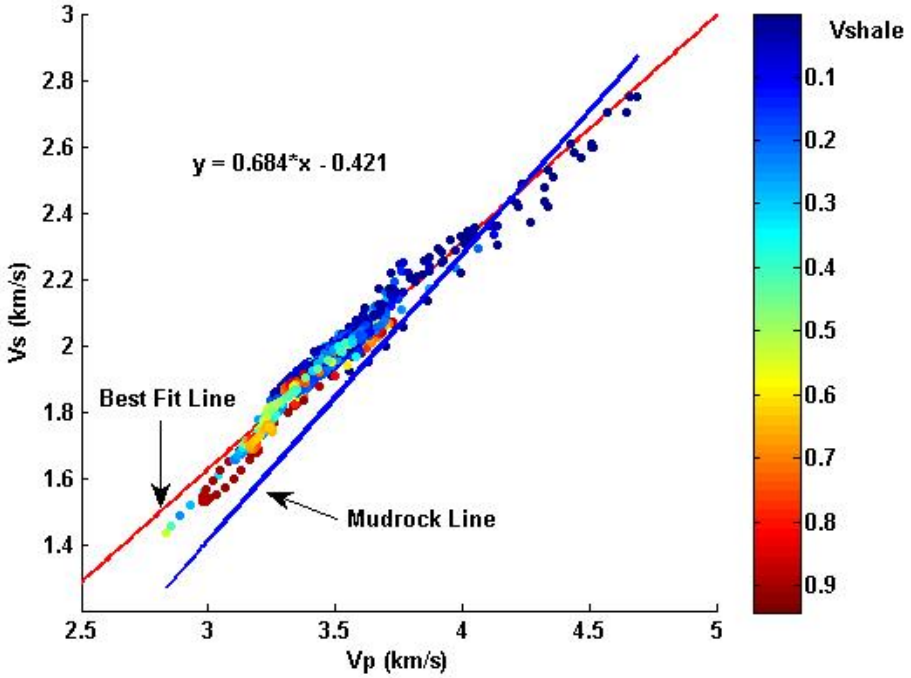

Figure 31: Local mudrock trend using measured Vp and Vs at well #1. Data are color coded by shale volume.

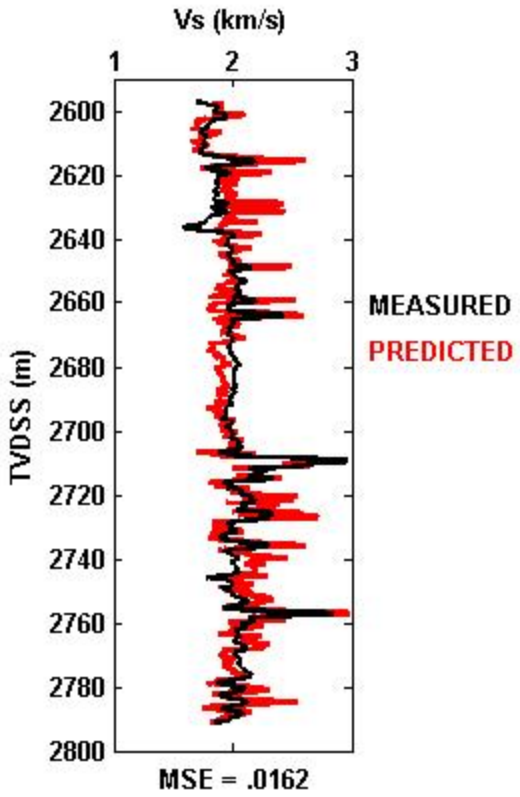

Figure 32: Vs prediction at well #2 using the locally derived mudrock trend at well #1. The MSE is .0162.

5.5 Greenberg-Castagna (GC) Empirical Formula

As with the mudrock line, the GC formulation was derived on water-saturated rocks. Therefore, Vs prediction using the GC formulation was also done using the fluid-substituted Vp (Figure 33). We see that the GC prediction provides a similar match to the locally derived mudrock trend and also underpredicts Vs in the clean sand interval.

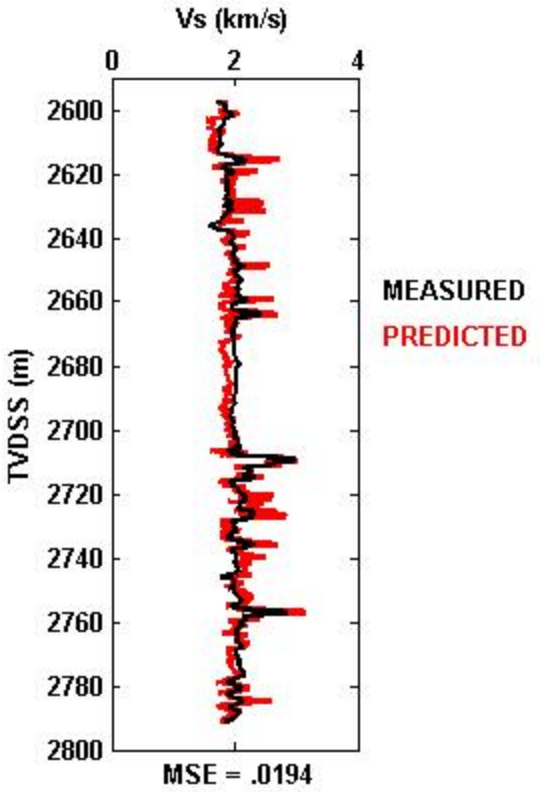

Figure 33: Vs prediction at well #2 using the GC formulation. MSE is .0194.

5.6 Non-Vp Regressions

The Tosaya, Castagna, Han, and Eberhardt-Phillips regressions described in section 3.2.6 were also tested at well #2. The pore pressure profile for this well can be found in table 3. The prediction results using these regressions are given in figure 34. Also, plotted in this figure in the 5th column is the prediction using a regression of Vs to porosity and shale volume derived at well #1. The local regression equation is:

$$Vs\left(\frac{km}{s}\right) = 2.3443 - 1.3686\varphi - .4307X_{cl} \qquad (22)$$

where φ = porosity and X_{cl} = clay volume. In this case, shale volume is assumed to equal clay volume. As with well #1, the Han regression provides the best fit with an MSE of .0705, followed by the Eberhardt-Phillips regression (MSE=.1003), Tosaya regression (MSE = .1243), and the Castagna regression (MSE = .2028). However, the newly derived clay-porosity regression from well #1 provides a much better fit with an MSE of .0166.

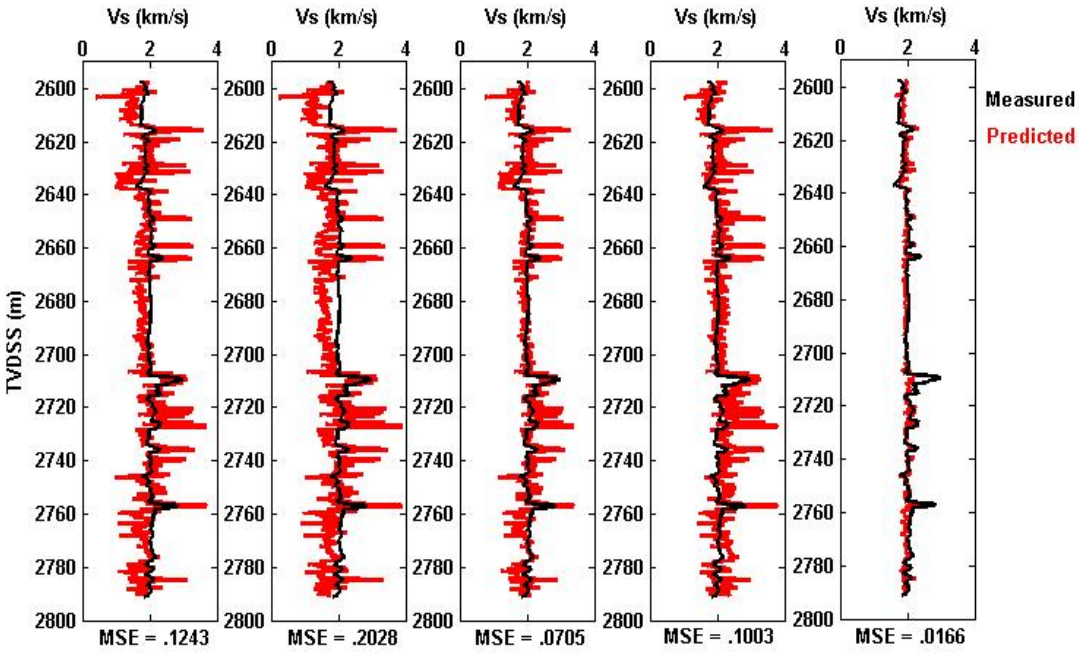

Figure 34: Vs prediction for well #2 using the non-Vp regression equations. The predictions from left to right are based on equations (16), (17), (18), (19), and (22). Equations and coefficients for the first four equations are given in section 3.2.6. MSE is .1243, .2028, .0705, .1003, and .0166, respectively.

5.7 Raymer-Hunt-Gardner (RHG) Vs Equation

The Raymer-Hunt-Gardner equation Vs equation was described in section 3.2.7. The method was utilized at well #2 in the same manner as well #1, using the elastic

moduli inverted from Vp using the Krief model. Matrix shear modulus was found using the Voigt-Reuss-Hill average. Prediction results are shown in figure 35. Overall, the prediction is relatively accurate with an MSE of .0906, however it is not as good as the prediction at well #1 using this model which had an MSE of .0462. This is, in part, probably due to errors in fluid saturation and fluid density as this well is not fully brine saturated. However, this model has the advantage of being applicable to wells with any pore fluid.

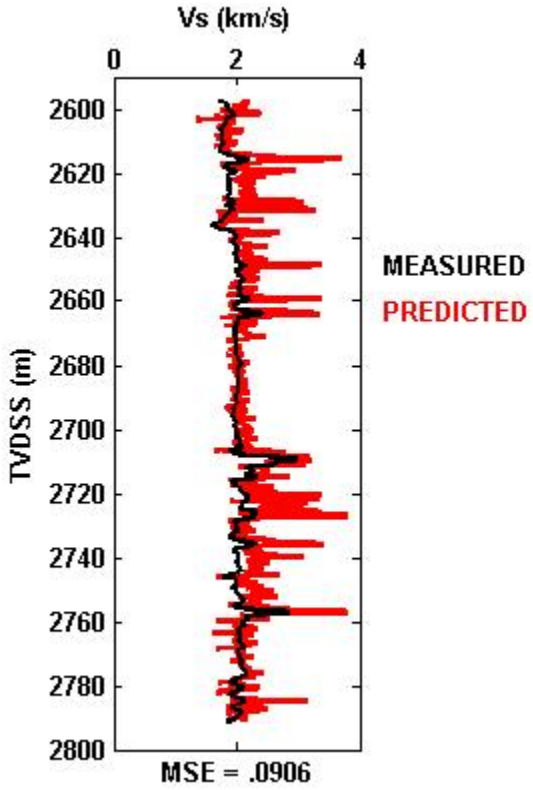

Figure 35: Vs prediction results at well #2 using the RHG Vs equation. MSE is .0906.

5.8 Summary

A summary of the results are provided in table 13.

Model	Mean Squared Error (MSE)	Correlation Coefficient (R^2)
Krief	**.1203**	**.4123**
Self-consistent (SC)	**.0632**	**.4354**
DEM	**.0883**	**.4087**
Mudrock Line	**.0378**	**.5882**
Locally Derived Mudrock Line	**.0162**	**.5882**
Greenberg-Castagna (GC)	**.0194**	**.6508**
Tosaya Regression	**.1243**	**.4251**
Castagna Regression	**.2028**	**.4048**
Han Regression	**.0705**	**.4174**
Eberhardt-Phillips Regression	**.1003**	**.4708**
Locally Derived Vshale-Porosity Regression	**.0166**	**.4237**
RHG	**.0906**	**.4274**

Table 13: Summary of Vs prediction results at well #2.

Chapter 6: AVO Modeling

It is well known that the reflection coefficient (amplitude) of a seismic wave varies with incidence angle (offset). This phenomena has been used extensively as a direct hydrocarbon indicator. Ostrander (1982) showed that high porosity gas sands with abnormally low Poisson's ratios have a noticeable effect on the amplitude variation with offset (AVO) response. Figure 36, taken from Rutherford and Williams (1989), shows the P-wave amplitude from a shale-gas sand interface for various normal incidence amplitude values. They classified the AVO response into three different classes. Class 1 are high impedance sands and show a decrease in positive reflection amplitude with offset. Class 2 are sands with impedance close to that of the encasing shale and are represented by a polarity change or slight increase in amplitude with offset. Class 3 are low impedance sands and show an increase in negative amplitude with offset.

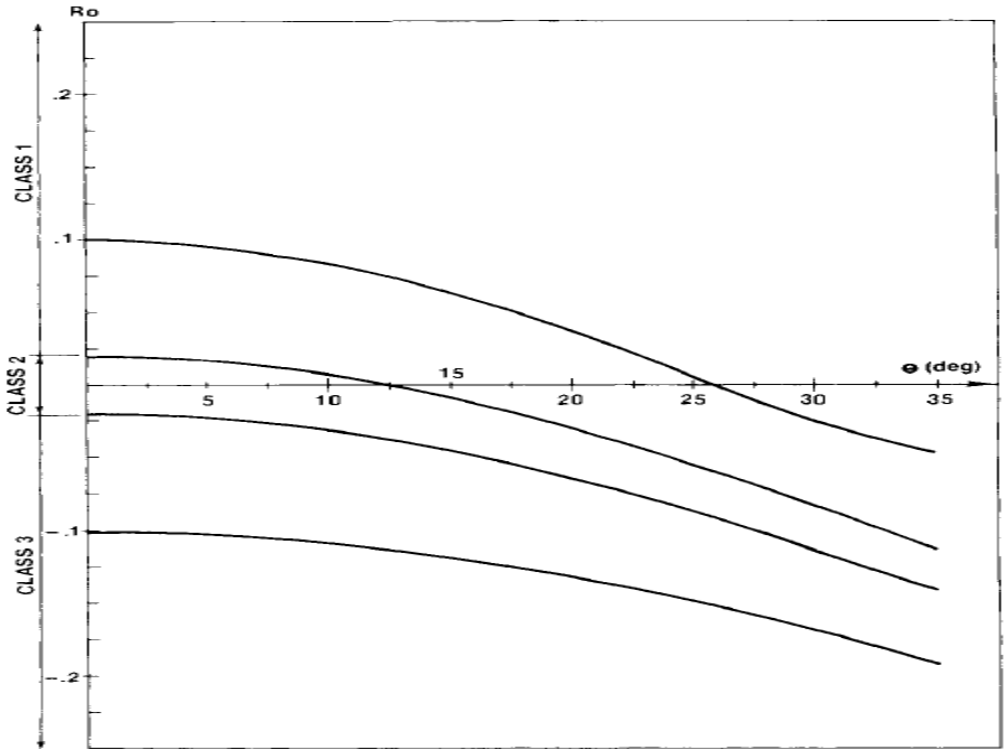

Figure 36: AVO response for a shale-gas sand interface for various normal incidence amplitude values with resulting AVO classes. Class 1: high impedance sands. Class 2: sands with impedance close to that of the shale. Class 3: low impedance sands. Taken from Rutherford and Williams (1989).

Aki and Richards (1980) derived a form of the reflection coefficient as a function of offset that is parameterized by P-wave velocity, S-wave velocity, and density. Shuey (1985) presented an alternate form of their approximation, with separate terms representing a different angular range of offset. The Shuey approximation in its full form is provided in appendix C.

Here we use the Shuey approximation to model the AVO response at a shale-sand interface. The overlying shale properties are representative of Norne Field and are taken from Dadashpour (2009). The shale properties are:

- Vp = 3.35 km/s
- Vs = 1.8 km/s
- Density = 2.45 g/cc.

The Tofte formation was chosen as the sand model and the AVO responses were tested using the various Vs predictions in the previous chapter. The MSE, as well as the percent difference from the measured Vs, was calculated for the Tofte formation alone so has to have an accurate comparison between the Vs prediction models and their AVO response for this particular interval. The calculations in well #2 were restricted to the oil-saturated interval of the Tofte formation. The results for well #1 are given in table 14, and in table 15 for well #2. The average measured Vp, Vs, and density for the Tofte formation in each well are:

- Vp = 3.5564 km/s (well #1)

  3.2954 km/s (well #2)
- Vs = 2.0156 km/s (well #1)

  2.0069 km/s (well #2)
- Density = 2.2633 g/cc (well #1)

  2.2055 g/cc (well #2)

All transmission, overburden, anisotropy, etc. effects are not accounted for in this modeling so as to provide a simple, quantitative comparison. The AVO modeling results using the measured data is provided in figure 37. As well #1 is a shale-brine sand interface, we only see a slight increase in negative reflection amplitude with offset. On

the other hand, well #2 is a shale-oil sand interface and shows a larger increase in negative reflection amplitude with offset.

Model	Mean Squared Error (MSE)	Vs (km/s)	% Diff from Meas.
Krief	**.0303**	**2.0526**	**1.8**
Self-consistent (SC)	**.0354**	**2.1434**	**6.3**
DEM	**.0902**	**2.2582**	**12.0**
Mudrock Line	**.0176**	**1.8936**	**- 6.0**
Greenberg-Castagna (GC)	**.0024**	**1.9920**	**- 1.2**
Tosaya Regression	**.0411**	**2.0566**	**2.0**
Castagna Regression	**.0708**	**1.9277**	**- 4.4**
Han Regression	**.0334**	**2.1356**	**6.0**
Eberhardt-Phillips Regression	**.0907**	**2.2360**	**10.9**
RHG	**.0199**	**2.0047**	**- .0.5**

Table 14: Vs prediction results in the Tofte formation at well #1. Average measured velocity is 2.0156 km/s.

Model	Mean Squared Error (MSE)	Vs (km/s)	% Diff from Meas.
Krief	**.0537**	**2.0473**	**2.0**
Self-consistent (SC)	**.0258**	**2.0791**	**3.6**
DEM	**.0447**	**2.1425**	**6.8**
Mudrock Line	**.0582**	**1.7908**	**- 10.8**
Locally Derived Mudrock Line	**.0117**	**1.9300**	**- 3.8**
Greenberg-Castagna (GC)	**.0210**	**1.8981**	**- 5.4**
Tosaya Regression	**.0848**	**1.8192**	**- 9.4**
Castagna Regression	**.2161**	**1.6309**	**- 18.8**
Han Regression	**.0280**	**1.9603**	**- 2.3**
Eberhardt-Phillips Regression	**.0555**	**2.0696**	**3.1**
Locally Derived Vshale-Porosity Regression	**.0066**	**1.9376**	**- 3.5**
RHG	**.0371**	**2.0719**	**3.2**

Table 15: Vs prediction results in the Tofte formation at well #2. Average measured velocity is 2.0069 km/s

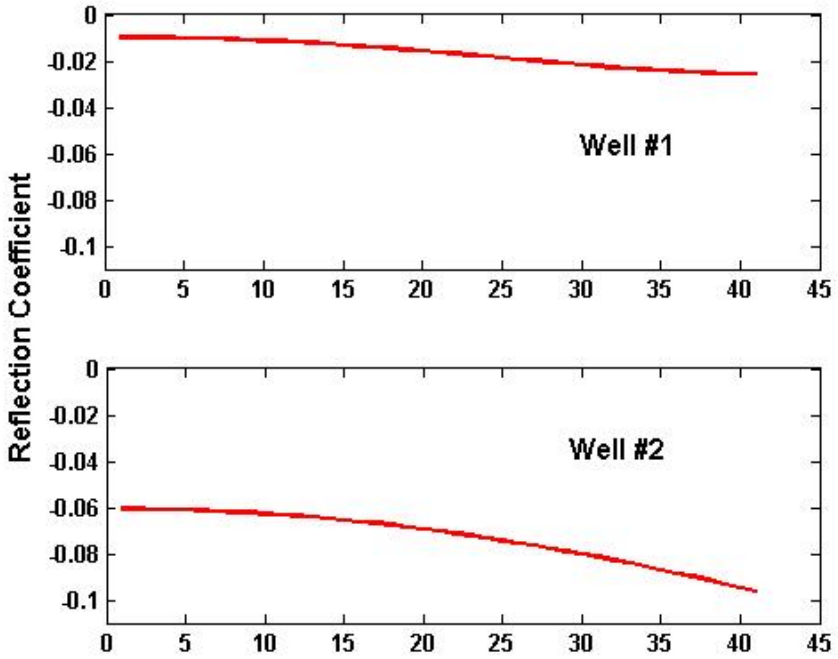

Figure 37: AVO modeling results for well #1 and #2 using the measured velocities and densities.

Using the predicted Vs results for each well, the AVO response was calculated and compared to the response using the measured data. Figure 38 shows the results for the 10 predictions made at well #1. Of the models that utilized the genetic algorithm, we see that the Krief prediction provides the closest match to the true modeled response. We don't see a noticeable difference in amplitude until around 30 degrees of offset. The SC and DEM models provide a larger AVO response than the measured results, with the SC model showing a better match than the DEM model. The AVO response between predicted and measured begins to separate around 15 degrees offset for the SC velocity and around 10 degrees for the DEM velocity.

Vs predicted using the mudrock line was lower than the measured velocity and thus the AVO response shows an opposite trend from the measured response. At around 15 degrees offset, the mudrock AVO response begins to show a decrease in amplitude with offset. The Greenberg-Castagna prediction provided an excellent match to the measured velocity and thus we see an almost identical AVO response to the measured results.

Of the non-Vp regressions, the Tosaya regression provides the best AVO match, with only a slight discrepancy at large offsets. The Castagna regression shows an opposite AVO response beginning at around 20 degrees but at a lesser magnitude than that provided by the mudrock prediction. The Han regression shows a larger AVO response, similar in magnitude to the SC model, while the Eberhardt-Phillips shows a much larger AVO response in a similar fashion to the DEM model.

The AVO model using the RHG predicted Vs provides the best match to the measured response, with no noticeable discrepancies between the two throughout the entire offset range. As the shear moduli used in the RHG prediction were derived from Vp inversion using the Krief model, this shows the effectiveness of the use of a genetic algorithm to invert for elastic moduli using the Krief model.

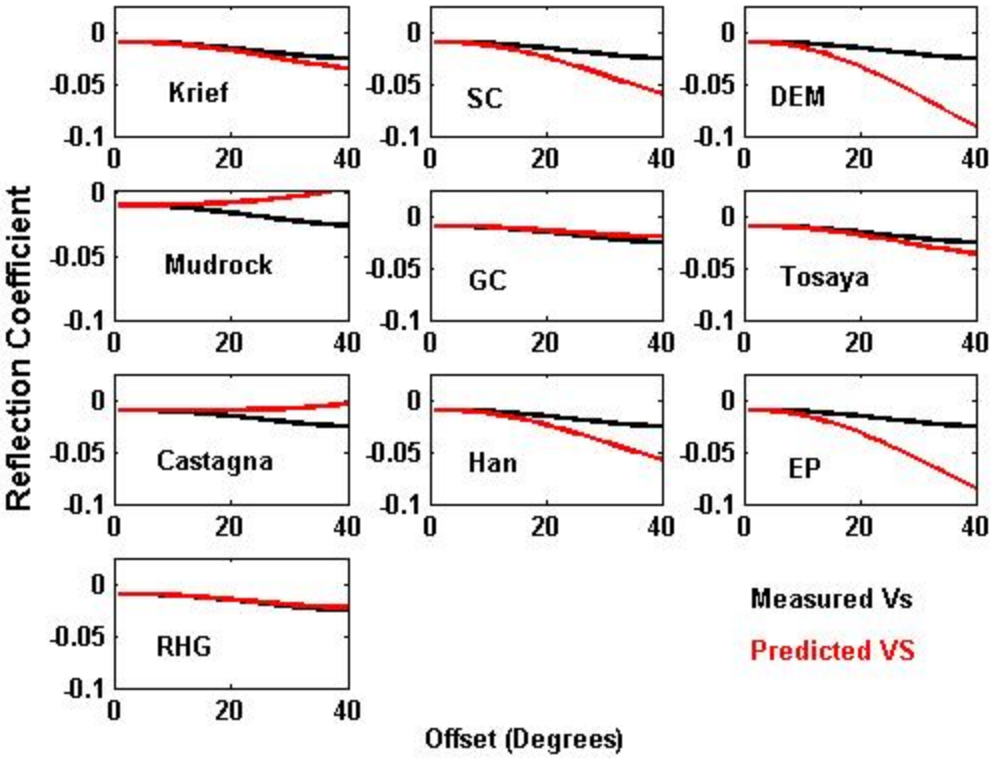

Figure 38: AVO modeling results at well #1 using predicted Vs.

Figure 39 shows the results of AVO modeling using the 12 Vs predictions at well #2. Once again, the Krief prediction provides the best match of the effective medium models to the true model. The SC model provides a relatively good match to the measured model, with separation between the AVO responses beginning at an offset of around 20 degrees. The DEM model shows a similar AVO mismatch as the SC model but at a larger magnitude and beginning at an offset around 15 degrees.

As was the case with well #1, the mudrock predicted Vs was lower than the measured Vs. As a result, we see an opposite trend from the true model, with the mudrock model showing a decrease in amplitude beginning at around 15 degrees. The

locally derived mudrock equation provided a much better fit, but with a smaller increase in amplitude with offset. The Greenberg-Castagna predicted Vs provided an AVO model that had almost no change in amplitude with offset and thus fails to capture the true AVO response.

Unlike well #1, where the Tosaya model provided the best AVO match, the Han and Eberhardt-Phillips regressions provided a better match at well #2. The Tosaya and Castagna regressions underpredicted velocity and provided an opposite trend in AVO response. The locally derived porosity-shale volume regression actually showed no improvement over the Han and Eberhardt-Phillips regressions.

Finally, the RHG predicted Vs once again provided a relatively good match to the true AVO model. Noticeable separation between the two AVO models begins around 20 degrees of offset, with the RHG model showing a slightly larger increase in amplitude with offset.

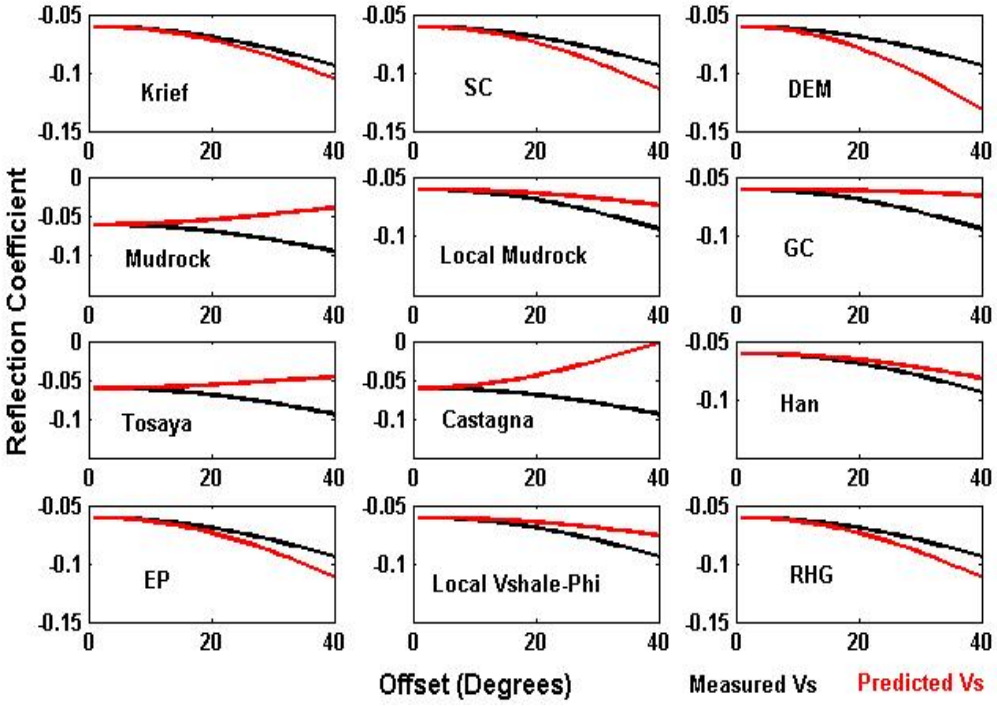

Figure 39: AVO modeling results at well #2 using predicted Vs.

Chapter 7: Discussion and Conclusions

Using only well log data, shear-wave velocity has been predicted using various models. We have shown that the use of a genetic algorithm can be used to invert for the elastic parameters of the logged interval and then those shear moduli used to predict Vs. In this environment, Vs prediction by Vp inversion was best accomplished using the Krief model. The Vp inversion method has the advantage of predetermination of the accuracy of the results by checking the Vp prediction results using the inverted moduli. Also, we can use this method in any pore fluid environment which makes it favorable over other models that have been derived in purely brine saturated conditions. The results were less accurate for the SC and DEM models, which had the added free variables of pore and grain geometries. The inversion for these geometry parameters is non-unique and thus without ground truth data as confirmation, the inverted geometrical factors cannot be assumed to be representative of in-situ conditions. The addition of core and thin section data would enhance the accuracy of the SC and DEM models and possibly make them reliable Vs log prediction models.

As expected, in the brine saturate well #1, the Greenberg-Castagna provided an excellent fit. However, the mudrock line, while showing a small MSE due to the less noisy nature of the prediction, underpredicted Vs enough to affect the AVO response. In well #2, the GC-predicted Vs did not predict Vs as accurately and resulted in an AVO response less accurate than the Krief model. Addition of Vs data from well #1 to assist in Vs prediction at well #2 enhanced the prediction over the non-local regressions, but their advantage in AVO modeling was negligible when compared to other models as seen in

figure 25. For both wells, the RHG model provided a good prediction and close AVO match, proving that this model can be a reliable predictor in any pore fluid environment.

In conclusion, in a brine saturated sand-shale environment, the Greenberg-Castagna formulation is probably the most reliable method of predicting Vs. However, if making a blind well prediction in a complex environment, inverting Vp for elastic moduli using the Krief model or prediction by the RHG model may be the best method. In a well with pore fluid other than brine, Vp inversion by the Krief model or the RHG Vs prediction is probably the most reliable method to predict Vs. We also see that the proper model is dependent on the Vs requirements. At well #2, we saw that the Krief prediction had a larger error than many of the other models when looking at the entire log interval while it had the most accurate AVO model when focusing on the Tofte formation. Thus, for AVO modeling a specific formation, Vp inversion using a genetic algorithm has shown to be the most effective method given the correct dry frame model is chosen.

References

Aki, K., and Richards, P.G., 1980. Quantitative Seismology: Theory and Methods: W.H. Freeman and Co.

Batzle, M. and Wang, Z., 1992. Seismic properties of pore fluids: Geophysics, **57**, 1396-1408.

Berryman, J.G., 1980b. Long-wavelength propagation in composite elastic media: J. Acoust. Soc. Am., **68**, 1809–1831.

Berryman, J.G., 1992b. Single-scattering approximations for coefficients in Biot's equations of poroelasticity: J. Acoust. Soc. Am., **91**, 551–571.

Castagna. J.P., 1985, Shear-wave time-average equation for sandstones: Presented at the 55th Ann. Internat. Mtg., Soc. Expl. Geophys., Washington, D.C.

Castagna, J.P., Batzle, M.L., and Eastwood, R.L., 1985. Relationships between compressional-wave and shear-wave velocities in clastic silicate rocks: Geophysics, **50**, 571–581.

Castagna, J.P., Batzle, M.L., and Kan, T.K., 1993. Rock physics – The link between rock properties and AVO response: Offset-Dependent Reflectivity – Theory and Practice of AVO Analysis, ed. J.P. Castagna and M. Backus: Investigations in Geophysics, No. 8, Society of Exploration Geophysicists, Tulsa, Oklahoma, pp. 135–171.

Chaveste, A., and Hilterman, F., 2007, Well-log inversion and modeling – A tool for understanding ambiguity and sensitivity of seismic data to changes in petrophysical properties: The Leading Edge, **26**, 812-817.

Chaveste, A. and Jimenez, J.R., 2003, Estimation of moduli and densities of rock constituents through global inversion of wire-line data. 73rd Ann. Internat. Mtg., Soc. Expl. Geophys., Expanded Abstracts, 1687-1690.

Dadashpour M, 2009. Reservoir characterization using production data and time-lapse seismic data, PhD dissertation, NTNU, Norway.

Dvorkin, J.P., 2008, Yet another Vs equation: Geophysics: **73**, 35-39.

Eberhardt-Phillips, D., Han, D.H., and Zoback, M.D., 1989, Empirical relationships among seismic velocity, effective pressure, porosity, and clay content in sandstone: Geophysics, **54**, 82-89.

Gassmann, F., 1951, Über die elastizität poröser medien: Vierteljahrss-chrift der Naturforschenden Gesellschaft in Zurich, **96**, 1-23.

Greenberg, M.L. and Castagna, J.P., 1992. Shear-wave velocity estimation in porous rocks: theoretical formulation, preliminary verification and applications: Geophys. Prospect., **40**, 195–209.

Han, De-hua, Nur, A., and Morgan, D., 1986, Effects of porosity and clay content on wave velocities in sandstones: Geophysics, **51**, 2093-2107.

Krief, M., Garat, J., Stellingwerff, J., and Ventre, J., 1990. A petrophysical interpretation using the velocities of P and S- waves (full-wave form sonic): The Log Analyst, Nov.-Dec., 355-369.

MATLAB user's guide

Mavko, G., Mukerji, T., and Dvorkin, J., 2009, The Rock Physics Handbook: Tools for Seismic Analysis of Porous Media: Cambridge Univ. Press.

Ostrander, W.J., 1984, Plane-wave reflection coefficients for gas sands at nonnormal angles of incidence: Geophysics, **49**, 1637-1648.

Pickett, G.R., 1963. Acoustic character logs and their applications in formation evaluation. J. Petrol. Technol., 15, 650–667.

Raymer, L.L, Hunt, E.R., and Gardner, J.S., 1980, An improved sonic transit-time-porosity transform: Soc. Prof. Well Log Analysts, 21st Annual Logging Symposium Transactions, Paper P.

Rutherford, S.R., and Williams, R.H., 1989, Amplitude-versus-offset variations in gas sands: Geophysics, **54**, 680-688.

Shuey, R.T., 1985, A simplification of the Zoeppritz equations: Geophysics, **50**, 609-614.

Smith, T.M., 2011, Practical seismic petrophysics: The effective use of log data for seismic analysis: The Leading Edge, **30**, 1128-1141.

Smith, T.M., Sondergeld, C.H., and Rai, C.S., 2003. Gassmann fluid substitutions: A tutorial. Geophysics: **68**, 430-440.

Statoil, 1999. Geological Report Norne Field. PL 128. Well 6608/10-E-3H.

Steffensen, I. and Karstad, P.I., 1996. Norne field development: Fast track from discovery to production in the Norne Field. JPT **48**: 296-299.

Tosaya, C.A., 1982, Acoustical properties of clay-bearing rocks: Ph.D. Thesis, Stanford Univ.

Verlo, S.B., and Hetland, M., 2008. Development of a field case with real production and 4D data from the Norne Field as a benchmark case for future reservoir simulation models testing. Masters Thesis, NTNU, Norway.

Wood, A.W., 1955, A Textbook of Sound. New York: McMillan Co.

Xu, S. and White, R.E., 1995. A new velocity model for clay-sand mixtures: Geophysical Prospecting, **43**, 91-118.

Appendix A: Petrophysical Log Derivation Parameters

Water-saturation (Sw) logs were derived using the Archie equation using the parameters listed in table A-1 (Statoil, 1999)

a	1.0
m	1.84
n	2.2 for Garn 3, Garn 2, Ile 2, Tilje 3, Tilje 2, Tilje 1 1.84 for Garn 1, Not, Ile 3, Ile 2, Åre. 2.02 for Tofte 4, Tofte 3, Tofte 2, Tofte 1
rw	0.054 Ohmm at 98°C
Rt	Deep Laterolog

Table A-1: Petrophysical parameters used to derive water saturation curves at Norne Field (Statoil, 1999).

Density porosity was calculated based on a core-log calibration using the equation:

$$PhiD = a + b * Rhob$$

where a and b are coefficients derived from a linear correlation between core and log data.

Appendix B: P and Q Geometrical Factors

The P and Q coefficients for arbitrary inclusion shape are given by (Mavko et al., 2005):

$$P = \frac{1}{3}\left(T_{iijj}\right)$$

$$Q = \frac{1}{5}\left(T_{ijij} - \frac{1}{3}T_{iijj}\right)$$

$$T_{iijj} = \frac{3F_1}{F_2}$$

$$T_{ijij} - \frac{1}{3}T_{iijj} = \frac{2}{F_3} + \frac{1}{F_4} + \frac{F_4F_5 + F_6F_7 - F_8F_9}{F_2F_4}$$

$$F_1 = 1 + A\left[\frac{3}{2}(f+\theta) - R(\frac{3}{2}f + \frac{5}{2}\theta - \frac{4}{3})\right]$$

$$F_2 = 1 + A\left[1 + \frac{3}{2}(f+\theta) - \frac{1}{2}R(3f+5\theta)\right] + B(3-4R) + \frac{1}{2}A(A+3B)(3 - 4R)[f + \theta - R(f - \theta + 2\theta^2]$$

$$F_3 = 1 + A\left[1 - \left(f + \frac{3}{2}\theta\right) - R(f+\theta)\right]$$

$$F_4 = 1 + \frac{1}{4}A[f + 3\theta - R(f-\theta)]$$

$$F_5 = A\left[-f + R(f + \theta - \frac{4}{3})\right] + B\theta(3-4R)$$

$$F_6 = 1 + A[1 + f - R(f+\theta)] + B(1-\theta)(3-4R)$$

$$F_7 = 2 + \frac{1}{4}A[3f + 9\theta - R(3f + 5\theta)] + B\theta(3 - 4R)$$

$$F_8 = A\left[1 - 2R + \frac{1}{2}f(R - 1) + \frac{1}{2}\theta(5R - 3)\right] + B(1 - \theta)(3 - 4R)$$

$$F_9 = A[(R - 1)f - R\theta] + B\theta(3 - 4R)$$

where A, B, and R are given by

$$A = \frac{u_i}{u_m} - 1$$

$$B = \frac{1}{3}\left(\frac{K_i}{K_m} - \frac{u_i}{u_m}\right)$$

$$R = \frac{1 - 2v_m}{2(1 - v_m)}$$

with subscript i representing the inclusion and subscript m representing the matrix.

θ and f are given by:

$$\theta = \frac{\alpha}{(1 - \alpha^2)^{\frac{3}{2}}}\left[cos^{-1}\alpha - \alpha(1 - \alpha^2)^{\frac{1}{2}}\right]$$

$$f = \frac{\alpha^2}{1 - \alpha^2}(3\theta - 2)$$

where α is the aspect ratio.

Appendix C: Shuey's Form of the Aki and Richards Approximation (Shuey, 1985)

$$R_{PP}(\theta_1) = R_P + \left(A_0 R_P + \frac{\Delta\sigma}{(1-\sigma)^2}\right) sin^2\theta_1 + \frac{1}{2}\frac{\Delta V_P}{V_{Pa}}(tan^2\theta_1 - sin^2\theta_1)$$

where R_p is the normal incidence reflection coefficient and A_0 and B_0 are given by:

$$A_0 = B_0 - 2(1 + B_0)(\frac{1-2\sigma}{1-\sigma})$$

$$B_0 = \frac{\frac{\Delta V_P}{V_{Pa}}}{\frac{\Delta V_P}{\Delta V_{Pa}} + \frac{\Delta\rho}{\Delta\rho_a}}$$

where:

$\sigma = \frac{\frac{1}{2}(\frac{V_P}{V_S})^2 - 1}{(\frac{V_P}{V_S})^2 - 1}$,

$\Delta\sigma = \sigma_2 - \sigma_1$,

$\Delta V_P = V_{P2} - V_{P1}$,

$V_{Pa} = (V_{P2} + V_{P1})/2$,

$\Delta\rho = \rho_2 - \rho_1$,

$\Delta\rho_a = (\rho_2 + \rho_1)/2$